Characterization of Bioparticulate Adhesion to Synthetic Carpet Polymers with Atomic Force Microscopy

A Thesis
Presented to
The Academic Faculty

By

Beng Joo Reginald Thio

In Partial Fulfillment
Of the Requirements for the Degree
Doctor of Philosophy in Chemical Engineering

Georgia Institute of Technology

December 2008

Characterization of Bioparticulate Adhesion to Synthetic Carpet Polymers with Atomic Force Microscopy

Approved by:

Dr. J. Carson Meredith, Advisor
School of Chemical & Biomolecular Engineering
Georgia Institute of Technology

Dr. Amyn Teja
School of Chemical & Biomolecular Engineering
Georgia Institute of Technology

Dr. Mark Prausnitz
School of Chemical & Biomolecular Engineering
Georgia Institute of Technology

Dr. Lawrence Bottomley
School of Chemistry and Biochemistry
Georgia Institute of Technology

Dr. F. Joseph Schork
School of Chemical and Biomolecular Engineering
University of Maryland

Date Approved: 24 October 2008

ACKNOWLEDGEMENTS

I owe the most to my advisor Dr. Carson Meredith as well as Dr. Santanu Chattopadhyay for the completion of this thesis. Through our conversations we came up with the research ideas and directions that evolved into the topic of this study. I am grateful to my advisor for his guidance and support in the past two years; Dr Chattopadhyay for teaching me the basic fundamentals of operating the AFM as well as the analysis of force-distance data. I would also like to thank Drs. Mark Prausnitz, Joseph F. Schork, Amyn Teja and Lawrence Bottomley for agreeing to serve on my committee; especially Dr Bottomley for his insightful comments on my AFM pollen force data and ways to improve on the control experiments. I am indebted to Yonghao Xiu and Jung Hyun Lee for getting me much needed SEM images of my AFM tip samples, Jung Hyun especially for getting me started on the AFM colloidal probe technique; Bernard Loo for agreeing to allow me to use the facilities at his advisor Dr. Bommarious' lab to grow my *E. coli* cells. I am also grateful to Kane Barker for helping me get an independent set of adhesion forces for the pollen humidity and compliance control experiments. Many thanks go to the Consortium on Competitiveness for the Apparel, Carpet, and Textile Industry (CCACTI) and the Carpet and Rug Institute for providing me with financial support for my graduate work.

Finally, I would also like to acknowledge my parents, especially my mother, for providing me with much needed long-distance emotional support and encouragement.

TABLE OF CONTENTS

List of Tables

List of Figures

SUMMARY

Particles originating from bacteria, fungi (including mold spores, mildew, yeast), pollen, dust mites, and viruses can induce immune responses that trigger allergies and asthma, if not outright infection. Carpeting is believed to act as a "sink" where bioparticulates are trapped via adhesive interactions and then are released by foot traffic or cleaning. This scenario can result in an accumulation of contaminants at higher levels than would be found outdoors or in a carpet-less environment. Numerous organizations (e.g., school districts, hospitals) have taken steps to remove carpeting[1-4], even though this hypothesis remains unproven. While statistical studies exist both in support and denial of the accumulation hypothesis, there is little fundamental understanding of the microscopic-level interactions between carpet and bioparticles. A fundamental understanding of particle affinities with polymers utilized in carpet would help to develop accurate models and address real problems in a rational and productive manner.

In addition, a solution to the bioparticulate accumulation problem would have a profound impact on US health, resulting in significant economic savings. More than 20 million people suffer from asthma in the U.S., with children being the most vulnerable. In 2000 there were 9.3 million physician office visits and 1.8 million emergency room visits due to asthma alone, resulting in an estimated $9.4 billion in medical costs and $4.6 billion in lost productivity annually.

In this thesis, two measurement techniques were developed to quantify the adhesive interactions between biological particulates and polymeric carpeting materials. Atomic force microscopy (AFM) was used to measure the adhesive interactions of relevant biological particulates (in this case the *E. coli* bacteria and *A. artemisiifolia* ragweed pollen grains) with Nylon-6 and Nylon-6,6, polyamide-12 and polystyrene. The adhesion force measurements were modeled using several adhesion theories. We found that the Hamaker models were sufficient for explaining the data, indicating the prominence of van der Waals forces in controlling bioparticle interactions with polyamides. In addition, the geometry of the pollen played a significant role: adhesion forces were approximately a multiple of the number of contact points the grain has with the surface. Forces for *E. coli* and polyamides were about the same magnitude as polyamide-polyamide surface self-interactions.

CHAPTER I

BACKGROUND

Aerial transmission of pollutants has serious implications for indoor air quality. The American Lung Association,[5, 6] the Environmental Protection Agency,[7] and others[8] have published numerous reports that point to interior carpeting and rugs as significant contributors to indoor air "pollution". Such pollutants include organic contaminants and particulate matter of both biological and non-biological origin.

Success of aerial transmission relies on the large numbers of particulates that are produced. It is the bioparticulates that are believed to be particularly aggravating to those who suffer from asthma, allergies, and other adverse lung conditions. Particles originating from bacteria, fungi (including mold spores, mildew and yeast), pollen, dust mites, and viruses can induce immune responses that trigger allergic and asthmatic reactions. Airborne fungal spores have been blamed for building-related illnesses. Typical concentrations of airborne biological particles indoors are within the range of 10-1000 m^{-3}, but may reach as high as 10^6 m^{-3} .[5]

Carpeting acts as a "sink" where bioparticulates are trapped via adhesive interactions, and then are released by foot traffic or conventional vacuuming [9, 10]. This scenario (Figure 1-1) results in an accumulation of particulate contaminants at higher levels than in a carpet-less environment.

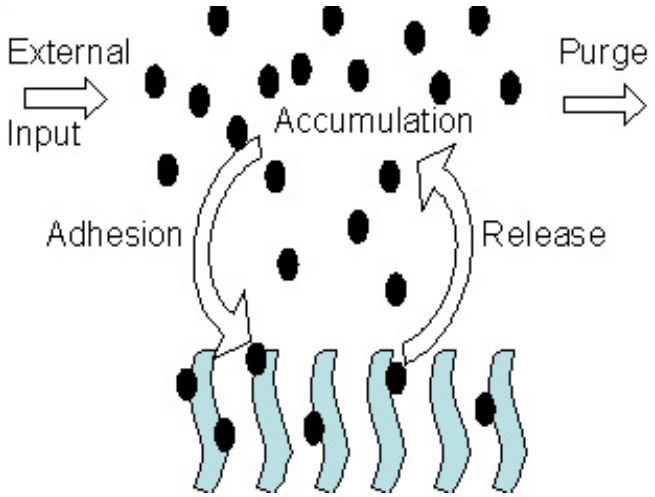

Figure 1 – 1. Schematic of adhesion-release-accumulation cycle for bioparticulates in carpeted environment.

However, it is not clear under what situations this accumulation cycle actually occurs to an extent that is harmful to indoor air quality. For example, recent studies have indicated that humidity, particle-type, carpet-type and cleaning methods have a profound impact on the outcome [5]. In fact, these factors may determine whether carpet is a help or hindrance to air quality. A solution to these problems based upon solid, fundamental measurements would have two positive impacts:

(1) the public perception and legal ramifications could be improved, and

(2) the health of millions suffering from allergies and asthma could be improved, along with significant economic savings.

Statistics surrounding these issues are readily available. For example, in 2001 more than 20 million people suffered from asthma in the U.S. alone [11]. Children between the ages of 5 and 17 had the highest rate [6]. In 2000, there were 9.3 million physician office visits, 1 million hospital outpatient visits and 1.8 million emergency room visits due to

asthma [6]. Other than being a potentially fatal condition to some people, asthma resulted in an estimated $9.4 billion in medical costs and $4.6 billion in lost productivity, including over 10 million lost school days annually at a cost of $1.4 billion [12]. Asthma is not the only health concern raised by bioparticulates. Infectious diseases such as influenza, measles, and chicken pox are also transmitted as indoor air pollutants, and molds and mildew can release disease-causing toxins.

Increasing attention has been focused on the quality of indoor air and its health implications. Air-tight buildings block out nature's ability to clean the air. Prior to the energy crisis, most homes were not particularly energy efficient. Small openings in the structure were usually left unsealed so fresh air passed freely through them, diluting and carrying indoor particulates.

The energy crisis of the 1970s led to a new building design philosophy in the United States. People were advised to insulate and make their homes more air-tight in order to conserve energy. One of the results of reducing the introduction of air into the house, and preventing the escape of conditioned or heated air, was a reduction in the ventilation of buildings and a corresponding decrease in the quality of indoor air. It is believed that resources saved on energy by making buildings more air-tight have been spent in part on medical bills for resulting health problems.

An inadequately designed air-tight building may suffer from deficient ventilation and increased moisture problems in the interior. Homes with increased relative humidity

suffer from a plethora of problems, not least of which is the provision of an environment in which an abundance of organisms can thrive. The presence of large numbers of micro-organisms and their debris, together with particulates of non-biological origin in the indoor air is often the source of disease in human beings through asthma, allergies and infections [13].

Allergy and asthma are closely related. Asthma is the most common chronic illness in childhood and is characterized by variable airflow obstruction with airway hyper-responsiveness. In the US, there has been an increase by about 100% in the incidence of asthma from 1980 - 1995 [14].

Carpet in its various forms has been a common indoor feature for many years. There are numerous advantages to having carpets in our homes and commercial spaces. These include their aesthetic appeal, comfort, economy, thermal and sound insulation properties as well as safety considerations. While there is some debate over which interior environment provides the main foci for bio-contaminants, it is generally accepted that carpets act as strong particle sinks. Carpet has been observed to have higher surface loadings of bioparticulate contaminants than tiled floors, while airborne levels were significantly higher over tiled floors [15].

One of the most common recommendations for persons with allergies and asthma is allergen avoidance. For this reason, health care practitioners generally recommend the removal of carpets. This recommendation is frequently made despite very little

knowledge about the difference between the accumulations of particulate contaminants in a carpetless versus carpeted environment. Carpet characteristics that influence its ability to act as a sink for particulates are also poorly understood [15]. Indeed, carpet is usually described as "wall-to-wall" or "fitted", with no mention of its age or condition, fiber content or construction characteristics.

Little consideration is given to the possibility that the presence of carpet may directly benefit some people in their homes. The primary goal of this thesis is to provide a methodology and initial data that can be used to identify the characteristics that control bioparticle adhesion. By identifying these characteristics it may be possible to design carpeting materials that improve indoor air quality. In addition, this data will help to dispel unfounded claims about carpet's role in the bioparticle accumulation process.

1.1 CARPET CHARACTERISTICS

1.1.1 COMFORT, THERMAL, AND ACOUSTICAL PROPERTIES

Carpets have been appreciated by many cultures over the centuries. Prior to the invention of the power loom by Erasmus Bigelow in America in 1839[16], woven carpets were mainly restricted to the upper class in society. Cham and Redfern[17] reported on the effect that flooring had on comfort and fatigue. They found that flooring properties do affect low back and lower leg discomfort/fatigue and that mats were almost always preferred over the hard floor control.

Carpets also play an important role in homes with their excellent sound absorbing ability [18]. The ability of a carpet material to absorb sound can be measured by its Noise Reduction Coefficient (NRC). It ranges from 0.0, indicating that no sound is being absorbed, to 0.99 meaning that almost all sound is absorbed. The NRC rating for carpets can be as high as 0.9. Carpets also have excellent thermal insulating properties [19]. Carpet fiber materials have low conductivity and do not readily transfer heat along the length of their fibers. Secondly, when they are spun into yarns, their fabric structure traps a large volume of air per unit weight. Air is an excellent thermal insulator.

1.1.2 ECONOMY

Carpet is an economical choice of floor covering material. This is one reason why seventy percent of the floors in the United States are covered with carpet [20]. In the 45-year period between 1950 and 1995, the cost of carpet increased by only 82.1%. During that same period, the combined cost of all commodities increased by 356.8% [21].

1.1.3 SAFETY

Carpets' fibrous nature meant that it is not slippery like hard ceramic tiles or concrete. They also provide some cushion support in the event of a fall. This meant improved safety in an environment for the elderly and the young. However, smaller

"throw rugs" can present a tripping hazard and caution should be taken when they are present in the house or commercial building.

1.2 SYNTHETIC CARPET FIBER MATERIALS

Synthetic carpet fibers are dominant in the fiber market, and are mainly made from nylon with 62.3% of the market share, polypropylene (or olefin) at 31.5% and polyester at 5.8% [21]. Wool constitutes the bulk of the remaining 0.4%, and is considered a luxury raw material. For this reason we decided to focus our studies on the two primary nylons used in carpet fiber: Nylon 6 and Nylon 6,6.

1.2.1 MATERIALS

1.2.1.1 NYLON

Nylon was discovered by researchers at DuPont in 1938. The Nylon 6,6 fiber used for carpet construction is transparent and readily magnifies the magnitude of soiling in carpets. Thus in the production of nylon fibers for carpet uses, the change in shape from round to trilobal or the addition of voids to a square shaped fiber are measures designed to reduce apparent soiling [22].

Nylon is popular because of its resilience and resistance to crushing and matting. It is resistant to stain penetration and dye fading due to sunlight or atmospheric contaminants.

There are two main types of nylon being used as carpet fiber materials – Type 6 and Type 6,6. They have dissimilar chemical compositions and are made from different raw materials (Type 6 – caprolactam; Type 6,6 – hexamethylene diamine and adipic acid). Structurally, Type 6,6 has twice the number of sites available for hydrogen bonding between the polymer chains than Type 6 [23]. Their chemical structures are shown in Figure 1 – 2.

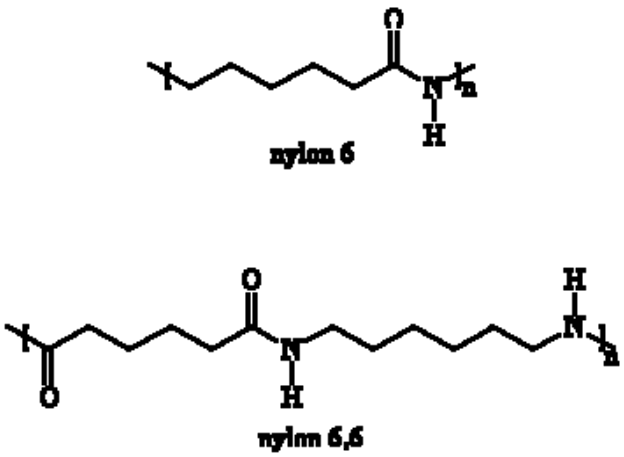

Figure 1 – 2. Repeating units of Type 6 and Type 6,6 nylon.

Thus Type 6,6 nylon has a tighter molecular structure with more hydrogen bonding. It is more crystalline. Molecular flexibility of Nylon 6 would render more of its polar groups to interact with any surface particle(s) which would in general give rise to stronger adhesive force.

The surface energies of the Nylons are of considerable importance to researchers given their incorporation into many consumer products either as stand-alone carpet fiber materials or in combination with other types of polymers in various composite materials such as tire cords, rubber or soil-resistant fluorocarbon coated carpet[24]. The surface energies of the polyamides come from the functional groups on the polymer surface. Methylene (-CH2-) groups constitute the dispersion component, and amine, carboxyl and amide (-NH2, -COOH, -CONH2-) groups contribute dispersion, polar dipole, and specific interaction (H-bonding or electron donor-acceptor) components of the surface energy. These functional groups play an important role in the adhesion of functional materials as in the case of the tire cords or soil release finishes in fluorocarbon-coated carpet. Most polymer pairs are immiscible at the molecular level and, as a result, form two or more phases upon blending. The mechanical properties of such blends depend, among other things, on the structure and mechanical strength of the interface between these different phases. Without additives, this interface is weak due to the lack of entanglements between the chains of both polymers. To enhance the interfacial adhesion of the polyamides with an immiscible polymer such as polystyrene (PS) or polypropylene (PP), chemical compatibilizers are often used in industry[25, 26]. Basically, such compatibilizers are small amounts of functionalized polymers which react with the two polymers at the interface to form *in-situ* copolymers. Their main advantage is that block copolymers do not need to be synthesized separately before blending to form the desired product. Thus, interfacial adhesion between the polyamide and PS can be improved with the addition of a styrene-maleic anhydride (SMA) copolymer which reacts easily with the

amine end group of the polyamide, and an analog exists for the polyamide with PP by incorporating a small amount of maleic anhydride functionalized PP. However, not much is known quantitatively about the adhesion forces between such polymer pairs. The polyamide-polystyrene adhesion forces are discussed in detail in Chapter III.

1.3 ALLERGIES, ASTHMA AND OTHER ADVERSE LUNG CONDITIONS

1.3.1 PATHOPHYSIOLOGY

Allergic reactions occur when a person, who has produced Immunoglobulin E (IgE) antibody in response to an innocuous antigen, or allergen, subsequently encounters the same allergen. The allergen triggers the activation of IgE-binding mast cells in the exposed tissue, leading to a series of responses that are characteristic of allergy [27].

Allergy is one of a class of four immune system responses classified by Coombs and Gell [27]. This is also known as a Type I hypersensitivity, an immune malfunction mediated by IgE. It results in an immediate-type systemic inflammatory response which has symptoms ranging from as mild as allergic rhinitis (or runny noses) to life-threatening anaphylactic shock and death [28].

Local symptoms are:

- Nose: swelling of the nasal mucosa (allergic rhinitis)
- Eyes: redness and itching of the conjunctiva (allergic conjunctivitis)
- Airways: bronchoconstriction wheezing and dyspnoea, sometimes outright attacks of asthma
- Skin: various rashes such as eczema, hives and contact dermatitis.

Systemic allergic response is also called anaphylaxis. Depending of the rate of severity, it can cause cutaneous reactions, bronchoconstriction, oedema, hypotension, coma and even death.

Hay fever is one example of an exceedingly common minor allergy - large percentages of the population suffer from hay fever symptoms in response to airborne pollen. Asthmatics are often allergic to dust mites. Apart from ambient allergens, allergic reactions can be due to medications [29].

Much human allergy is often caused by the uptake of limited amounts of small-protein allergens through inhalation or ingestion. These allergens reproducibly elicit IgE production in susceptible individuals. After IgE has been produced to respond to a specific antigen, the IgE antibodies attach themselves to the surface of mast cells and await the introduction of the specific antigen to which it responds. When the antigen appears, the IgE captures it and attempts to destroy it by releasing the chemical mediator, histamine, contained within the mast cell. Histamine and other mediators are responsible for the symptoms of an allergic reaction, such as swelling of the tissues, sneezing, wheezing, coughing, and other reactions [29].

The allergic reaction typically continues: these newly released mediators recruit other inflammatory cells to that site, resulting in additional inflammation. Many symptoms of chronic allergic disease - such as swelling, excessive mucus and hyper-

responsiveness to irritating stimuli are the result of tissue inflammation due to ongoing exposure to allergens [29]. It is not yet fully understood why some substances trigger allergies and others do not, nor why every person does not develop an allergic reaction after exposure to allergens. A family history of allergies is the single most important factor that predisposes a person to develop allergic disease. If one parent has allergic disease, the estimated risk of the child to develop allergies is 48%; the child's risk grows to 70% if both parents have allergies [29].

1.3.1.1 ALLERGEN AVOIDANCE/REMOVAL

Aside from immunological and pharmaceutical treatments beyond the scope of this thesis, a common treatment regime involves avoidance of allergenic materials. As stated earlier, in severe cases removal of carpeting is recommended by medical personnel. Persons with allergies are advised to avoid consuming foods to which they are allergic, to avoid contact with substances that are common allergens and are highly allergenic to, and to make environmental changes that will reduce the amount of allergen to which they are exposed. Additionally, some recommend the use of air filters, particularly a high-efficiency particulate-type air filter (HEPA) to remove air-borne allergens [30].

1.4 ATOMIC FORCE MICROSCOPY (AFM) AND RELEVANCE TO THIS PROJECT

The ambiguous relationship between carpeting and the indoor air quality/ allergic symptoms necessitate a scientific approach. Atomic Force Microscopy (AFM) will be adapted here to measure and quantify the adhesive interactions of a large range of relevant biological particulates with nylon and control materials.

No previous known work has investigated cell or bioparticle adhesion with a surface as complex as that of a typical nylon fiber encountered in carpeting. Model organisms such as the bacterium *E. Coli*[31] and *A. artemisiifolia*[32] ragweed pollen grains are chosen for a start as they have been studied quite extensively with regard to metabolism, replication and cell division. The former also has its entire genome mapped. In addition, these two organisms are among the most significant to health concerns.

Chapter II provides a broad overview and background of the atomic force microscopy techniques employed as well the theoretical adhesion models selected for use in the polymer – polymer and polymer – bioparticulate interactions. Chapter III discusses in detail the AFM – measured polymer-polymer adhesion forces and the applicability of the selected theoretical models in quantifying the forces. Chapters IV and V look at the application of the theoretical adhesion models with regard to the class of organisms (bacteria and pollen) interacting with the polymers and the reproducibility of the measured force data. Finally, Chapter VI concludes with the results of this PhD work and provides recommendations for future study in the area of polymer – bioparticulate adhesion.

CHAPTER II

FORCE SPECTROSCOPY USING AFM – MODELS AND CONSIDERATIONS

2.1 ATOMIC FORCE MICROSPECTROSCOPY (AFM) PRINCIPLE

Microscopy techniques can be broadly classified into two major groups. The first type is known as "far-field microscopy" because the distance between the sample and the point at which the image is observed is long compared to the wavelengths of the photons or electrons involved. The image obtained is in the form of a diffraction pattern and the resolution is limited by the wavelength of the incident beam on the target [33].

"Near-field microscopy" on the other hand includes a class of microscopes known as scanning probe microscopes (SPMs). They work on the principle of bringing a very sharp probe tip close to the sample surface. This probe measures the change in the intensity of a tip-surface "interaction signal". In closed-loop control, the signal is amplified and fed to a piezoelectric scanner to control the distance between the probe tip and the surface. The major advantage SPMs have over "far-field" microscopes is that they are not limited by the diffraction-related resolution [33]. The AFM is a form of SPM and was invented in 1986 by researchers at IBM [34]. AFM imaging is performed by sensing the force between a very sharp probe and the sample surface. An AFM image is thus generated by recording the force changes as the probe tip (or sample) is scanned in the x and y directions parallel to the surface. The force is monitored by attaching the tip

to the end of a thin, flexible cantilever connected to a piezoelectric scanner. Interaction forces between the tip and sample cause the cantilever to bend or deflect during the scanning. The magnitude of the force experienced by the probe will be proportionally determined by the deflection of the cantilever[35]. The deflection signal is acquired and digitized to provide a three-dimensional image of the surface.

The cantilever deflection is determined optically by means of a laser beam focused on the free end of the cantilever as illustrated in Figure 2-1. A photodiode acts as a detector for the reflected beam and the change in cantilever position in the z direction is recorded electronically. The change in height of the piezo is monitored by a PC based controlled feedback system and used to acquire topographic information. AFM cantilevers are typically made of silicon or silicon nitride by microfabrication techniques [35].

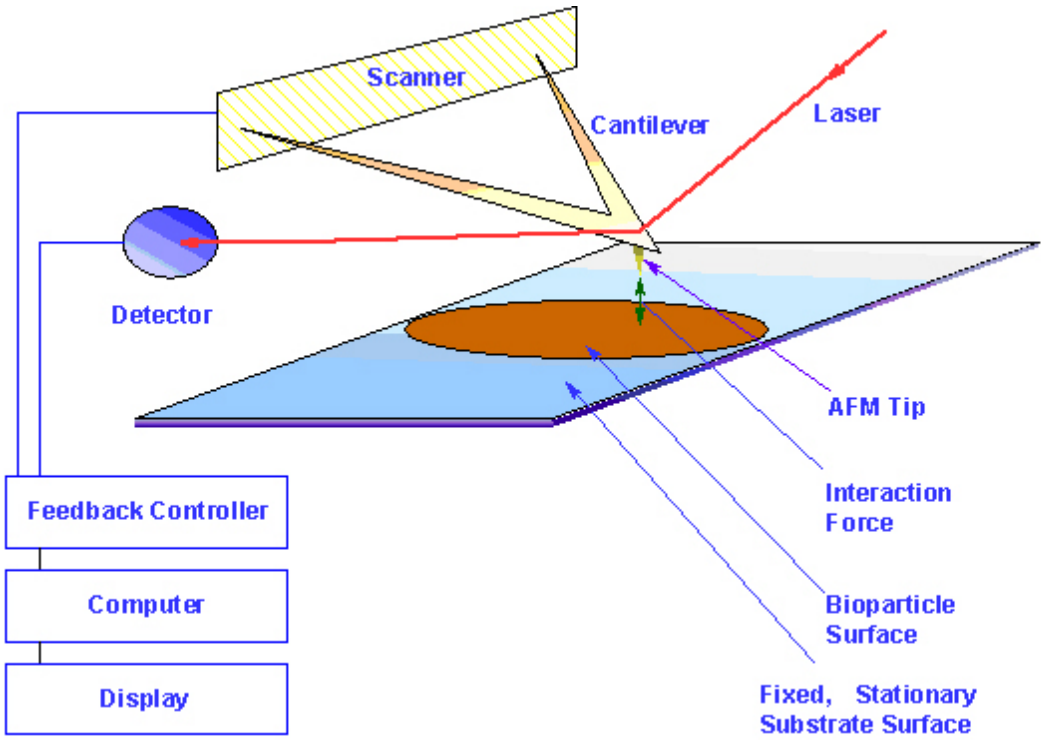

Figure 2 – 1. Schematic illustration of the AFM technique.

2.1.1 FORCE MEASUREMENT

The AFM's ability to measure localized force interactions between the probe tip and the sample surface was realized soon after its invention. The first applications were to measure surface forces on graphite and lithium fluoride [36].

To measure the force between the probe tip and the sample surface, a force-distance curve is recorded by monitoring the cantilever deflection as a function of the vertical displacement of the piezoelectric scanner at a fixed x, y position. This means that the probe tip is moved towards the surface in the Z direction (normal to the surface). After

contact has been established, the tip is slowly withdrawn from the surface until no interaction force is sensed between the tip and the surface [37].

A raw curve plot is that of the photodiode voltage against the scanner (Z) position. With the relevant correlations this plot can be converted into a force-separation-distance curve.

A typical example of an AFM force curve is given in Figure 2 – 2.

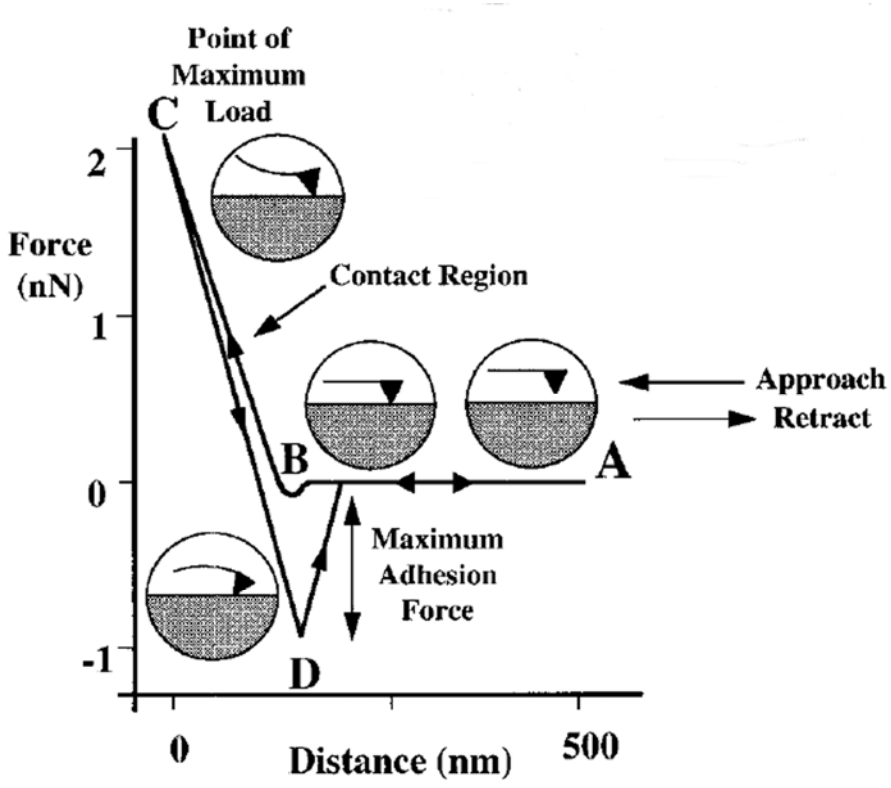

Figure 2 – 2. Schematic of a generic force-displacement curve for a contact-mode AFM [38].

During a force measurement cycle, the AFM tip is moved towards the surface (approach curve) at a constant velocity until it contacts the sample (B). The approach

section of the force-displacement curve can be used to measure surface forces such as van der Waals and electrostatic, solvation, hydration, and steric/bridging forces depending on the operating condition (air, solution) of the AFM [35]. The cantilever starts to bend as the tip is pressed against the surface. This continues until a pre-determined point of maximum load is reached (C). When the tip and the surface are in contact, the force curve can be roughly described by Hooke's law, $F = k\Delta Z$, where ΔZ and k are the deflection and the spring constant of the cantilever respectively [37]. When the force is increased in the contact region, the shape of the approach curve can be used for the determination of local elasticity properties such as the Young's modulus of the surface material.

The direction of motion is now reversed and the probe is withdrawn from the surface. This is also known as the retraction portion of the force curve. The tip is not immediately separated from the surface and the curve shows a hysteresis (D) often referred to as the adhesion "pull-off" force. Only when the elastic force pulling the tip away from the surface is equivalent to the adhesive force does the tip detach from the surface and returns to the original position at (A). This is of particular interest to this study as it serves as an estimate of the binding forces between the tip and the surface [35].

However, such force curve measurements have several limitations. Firstly, the determination of a "zero" Z position is purely arbitrary. The AFM does not conduct direct measurements of the distance between the sample and the tip. Secondly for "soft" surfaces, it is difficult to separate the relative contributions of the cantilever deflection from surface forces and the deformation of the sample under applied load [37].

2.2 FORCES BETWEEN PARTICLES

Adhesion forces arise because of interactions between the particle and a particular surface. The whole process is a complex and composite one as it is not only affected by fundamental forces between two molecules, such as van der Waals forces, but also by properties of the surface as a whole. These include surface energy and roughness. The types of interactions that are relevant to this study are described below. In general, these are Lifshitz – van der Waals attraction, capillary forces, and electrostatic forces [39]. When there is no electrical charging and relative humidity of the air is below 65%, the adhesion force can be regarded as mainly due to Lifshitz – van der Waals forces [40], whereas capillary forces dominate at relative humidity above 65% [41].

2.2.1 VAN DER WAALS FORCES

Van der Waals forces can be broadly divided into three groups – Debye, Keesom and London forces. London (or dispersion) forces between atoms and molecules and are always present[42]. This is in contrast to the other two types of forces which arise from electrostatic interactions involving charged or polar molecules. Thus Debye and Keesom forces may or may not be present depending on the properties of the molecules of our selected system. However, when present, Debye and Keesom forces often dominate the London forces, especially for highly polar molecules.

London forces occur between uncharged, non-polar molecules and arise because of fluctuations of the positions of the electrons orbiting about the nuclear protons. These generate transient dipoles which give rise to an electric field that polarizes and induces a dipole in any nearby neutral atom or molecule. The resulting interaction between the two dipoles leads to a temporary attractive force between the two molecules. Continuous changes in the electrons' positions will lead to a continual change in dipole moment of the first molecule. Consequently, the second molecule's dipole will follow[42]. The strength of interaction between the two molecules will be inversely proportional to inverse 6th power of their separation distance. Mathematically, this can be expressed as

$$w(r) = \frac{-C_{disp}}{r^6} \qquad (2\text{-}1)$$

where C_{disp} is the Coulombic dispersion energy potential. The negative sign indicates that this is attractive.

London forces have a number of characteristics:

a. They are considered long range forces compared to covalent bonds and are effective from distances greater than 10 nm to sub-interatomic spacing of 0.2 nm.
b. Depending on the situation, they may be attractive or repulsive and in general simple power laws do not apply to their dependence on separation distances.
c. They have an orienting effect on the affected molecules but this is usually weak compared to other intermolecular forces.

d. The interactions are *non-additive*, and this means the dispersion interaction of two bodies are affected by the presence of other bodies nearby.

The interaction energy (W) or work of adhesion of a sphere near a planar surface can be calculated by integrating the energies of all the atoms in a single body with all the atoms in the other. This is represented by

$$W = \frac{A_H}{12\pi D_0^2} \qquad (2\text{-}2)$$

where R is the radius of the particle, D_0 is the separation distance between the particle and surface and A_H is the non-retarded Hamaker constant, which is calculated by the equation

$$A_H = \pi^2 C \rho_1 \rho_2 \qquad (2\text{-}3)$$

where C is the interaction constant, and ρ_1 and ρ_2 are the number densities of the two interacting surfaces[42].

Equation (2-3) ignores the influence of neighboring atoms on the interaction between any pair of atoms. They could possess different electronegativities or polarizabilities and these would increase the contribution of Debye (induced dipole – induced dipole) and Keesom (dipole – dipole) forces. Furthermore, the additivity

approach cannot be readily extended to bodies interacting in a condensed media[42]. To solve this problem, Lifshitz made use of quantum field theory [43].

2.2.2 LIFSHITZ THEORY

A detailed discussion of the Lifshitz theory would require a strong background in quantum field theory and is outside the scope of this study. A simple explanation is that it offers an alternative method of calculating the non-retarded Hamaker constant in equation (2-3) that accounts the problem of additivity. In this theory, large bodies are treated as continuous media. The resultant forces between the large bodies are considered to be due to the fluctuations in electron density which lead to the temporary shifts in dipole moments. The electric field thus varies with time. If this field is assumed to be acting over a relatively long distance, interactions with other atomic electric fields and thus attractive forces between solid bodies will be possible[42].

Lifshitz theory does have its limitations. It does not take into account the separation distances at the molecular level and it assumes that the physical properties of the interacting bodies are uniform throughout [44].

All types of van der Waals forces are affected by the material properties as well as their contact geometry. This will mean the adhesion strength will vary accordingly. Important properties that will affect adhesion include elasticity, the true area of contact and surface roughness [45].

Israelachvili had simplified Lifshitz's theory for use in a system where two macroscopic phases interact across a third phase (i.e. the medium). This Hamaker constant consists of two terms, $A_{v=0}$ and $A_{v>0}$, which corresponds to the dipole-dipole/ dipole-induced-dipole contributions and the London dispersion contributions respectively.

$$A_H = A_{v=0} + A_{v>0} \qquad (2\text{-}4)$$

The simplified theory makes use of the respective static dielectric constants (ε_1, ε_2, ε_3) and the optical refractive indices (n_1, n_2, n_3) as follows:

$$A_H \approx \frac{3}{4}kT\left(\frac{\varepsilon_1-\varepsilon_3}{\varepsilon_1+\varepsilon_3}\right)\left(\frac{\varepsilon_2-\varepsilon_3}{\varepsilon_2+\varepsilon_3}\right)+\frac{3h\nu_e}{8\sqrt{2}}\left(\frac{(n_1^2-n_3^2)(n_2^2-n_3^2)}{(n_1^2+n_3^2)^{1/2}\{(n_1^2+n_3^2)^{1/2}+(n_2^2+n_3^2)^{1/2}\}}\right) \quad (2-5)$$

where v_e, the electronic absorption frequency is taken to be the same for all three components ($v_e = 3 \times 10^{15}$ Hz)[42, 46].

Equation (2-5) suggests that equivalent dielectric constants of the probe tip, the sample and the interacting medium would lead to the elimination of the first term. The dispersion contributions (as determined by the optical refractive indexes) would then be dominant in the tip-sample adhesion. If the refractive index of the medium (n_3) is

intermediate between the two phases, a negative van der Waals interaction may occur [47, 48].

Thus there is a need for a suitable choice of medium in this research study to avoid possible complications in the use of Equation (2 – 5). For my work, complications are minimized since air is used as the medium; air has a lower dielectric constant and refractive index compared to the materials used as the probe tip and sample surface.

2.2.3 CAPILLARY FORCES

Capillary forces are caused by the condensation of water at the point of contact between particles or inside the pores of hydrophilic materials. The presence of water will result in the formation of a meniscus. In the case where the particle (or probe tip) is hydrophilic, the water will wet the surface because it is energetically advantageous as compared to the water-air contact. This will create relatively large, often undesired forces between the surface and the particle (or probe tip) [39]. The value of this force depends on a multitude of factors including surface free energy, surface roughness, gap geometry, surface chemical condition and the meniscus curvature [49, 50].

The condensation of moisture on the materials may also lead to a physical effect. The contact surfaces may dissolve in the presence of water if the material is soluble. Crystallization may occur if the material surfaces are subsequently dried and this would affect adhesion forces between the particle and the surface. The water may also plasticize

hygroscopic materials and cause them to deform easier under an applied load. This would lead to an increase in the contact area and thus increase the adhesion force. Moisture can also act as a lubricant to ease the detachment of portions of the surface from that of the particle [39].

2.2.4 COULOMB (OR ELECTROSTATIC) FORCES

Coulomb forces arise from the electrostatic charging of surfaces and these can be either attractive or repulsive. They are most often created from friction [51]. When a charged particle is brought near a neutral surface, an equal but opposite charge will be induced on the surface. This creates an attractive force, and can be expressed as

$$F \alpha \frac{Q_1 Q_2}{d^2} \qquad (2\text{-}6)$$

where Q_i is the charge on the particle and d the distance between the centers of the charges. These forces are minimized by the presence of water (non deionized), which helps to conduct the static charges away.

For sphere-on-planar geometry, the force-distance relationship depends on the relative values of the distance D and sphere radius R. Equation (2-6) is usually valid for relatively long range separation distances. Equations (2-7) and (2-8) are usually more appropriate for the sphere-plane cases.

$$F = \pi \varepsilon_0 V^2 \frac{R}{D} \qquad \text{for } R >> D \qquad (2\text{-}7)$$

and

$$F = \pi \varepsilon_0 V^2 \left(\frac{R}{D} \right)^2 \qquad \text{for } R << D \qquad (2\text{-}8)$$

where V is the tip-surface potential difference [49].

2.2.5 OTHER FACTORS

2.2.5.1 SURFACE ROUGHNESS

Adhesion forces are strongly dependent on the surface roughness of the sample and the particle (probe tip). Consider the case of a particle resting on a 'rough' surface. If it is smaller than the distance between the 'hills' or 'crests' it will settle to the 'valleys'. This will mean an increase in the contact area and will lead to an increase in the adhesion force. The valleys also provide protection from the lateral forces that might be present to remove the particle. On the other hand, there will be reduced contact between the surface and the particle if the particle is larger that the 'wavelength' of the rough surface. This will mean a smaller van der Waals contribution to the adhesion force. Figure 2 – 3 shows a graphical effect of surface roughness on particle adhesion.

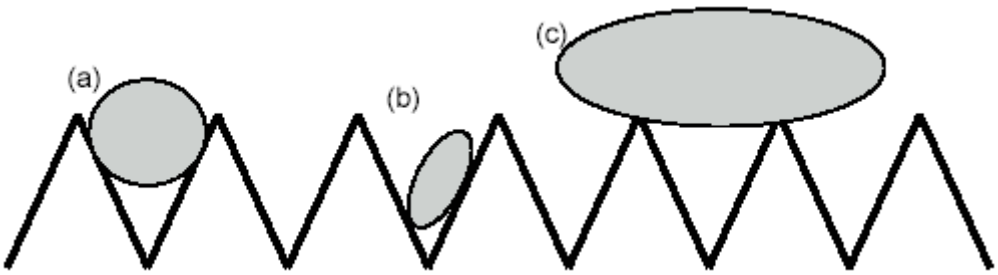

Figure 2 – 3. The effect of surface roughness on particle adhesion. In the first two cases (a, b), the particle is wedged between two 'hills' while in the third case (c) it is placed on top of the surface. The adhesion force is stronger in the first two and weaker in the last one than if it is placed on a flat or smooth surface [45].

The presence of surface roughness can result in huge discrepancies between predicted and actual adhesion forces [52].

2.2.5.2 SURFACE ENERGY

In a bulk phase of similar molecules, any molecule in feels a zero net force. However, in the event that a molecule finds itself at the phase boundary, e.g., a liquid-vapor boundary, it will feel a net attractive force towards other similar molecules in the liquid phase. This produces is a state of tension as a force is trying to contract the (liquid) surface.

If the bulk phase is liquid, the phenomenon is known as *surface tension*. In general, the greater the proportion of polar groups (e.g. O-H) in the bulk phase, the stronger the attractive forces amongst the molecules. Strong attractive forces produce high surface tension and a tendency to form discrete spherical droplets rather than wet the surface the liquid comes into contact with.

If the bulk phase is solid, this is known as *surface energy*. It describes the work done in overcoming the surface tension forces of the liquid and causing it to spread out rather than coalesce into droplets. Quantitatively, it is defined as the amount of work required to increase the surface area of a substance by 1 m^2 [53].

The terms *surface energy* and *surface tension* and their quantitative values are equivalent when applied to the case of liquids. This does not apply for solids. The forming of a new solid surface is due to two processes running consecutively. The phase is first cleaved and then subsequently rearranged to form the most stable configuration. Molecules in the liquid state are able to perform these simultaneously, while solid molecules are held in a rigid state and thus unable to rearrange in a short time-span. Liquids are typically at equilibrium and solids are not – the timescale and length scale for re-arrangement between the former and the latter are several orders of magnitude different. Their density may vary from the most stable state to a metastable state or an unstable state. Local changes in surface energy may occur as the surface area is increased or decreased with no corresponding change in molecule number [53].

2.2.5.3 SURFACE HARDNESS AND ELASTICITY

The hardness of a material surface is defined by its resistance to indentation [54], while elasticity is simply its ability to return to its initial state after the removal of an applied stress. For many materials, there exists a linear relationship when stress is plotted

against strain in the Hooke's law region [55]. The rate of change of stress with strain is known as the Young's modulus [56].

These two properties will largely determine how the particle (or probe tip) and the surface will deform on contact under an applied load. The extent of deformation will increase the contact area, and this can lead to a greater than predicted adhesion force [45, 52].

2.3 THEORETICAL ADHESION MODELS

2.3.1 HERTZ THEORY

Many models that describe adhesion force interactions between two solid spheres are derived from an analysis by Hertz in 1882 [57]. He considered two smooth elastic bodies in contact under an external load but ignored the attractive inter-particle surface forces. At high load P_0, the elastic deformation between the two bodies can be related to the radius a_0 of the circle of contact by

$$a_0^3 = \frac{3}{4}\pi(k_1 + k_2)\frac{R_1 R_2}{R_1 + R_2}P_0 \qquad (2-9)$$

where k_1 and k_2 are the elastic constants of the material of each sphere; which is

$$k_1 = \frac{1-\nu_1^2}{\pi E_1} \quad (2\text{-}10) \text{ and } \quad k_2 = \frac{1-\nu_2^2}{\pi E_2} \qquad (2-11)$$

where v is the Poisson ratio and E the Young modulus of each material [58].

There are several principal assumptions for Hertz's theory [59]. They are

a. a normally loaded contact exists between the bodies,
b. the material behaves as a linear elastic body,
c. the radius of contact area is small compared with the radius of the sphere,
d. there is frictionless contact between the surfaces resulting in the transfer of only normal stresses between the contacting surfaces.

The main drawback for the Hertz theory was summarized by Johnson et.al [58]. Larger than predicted contact areas between spherical bodies were measured at low loads. These suggested attractive adhesion forces were operating between the solids. At high loads, these forces are relatively insignificant but are not negligible as the loads are reduced towards zero.

Two models have been widely adopted to correct for the behavior of Hertzian contacts by including the effects of surface forces. They are usually described by the model of Johnson, Kendall and Roberts (JKR) [58] or by the model of Derjaguin, Muller and Toporov (DMT) [60].

2.3.2 JOHNSON, KENDALL AND ROBERTS (JKR) THEORY

The JKR theory is a modified form of Hertz Theory that included the thermodynamic work of adhesion for two adhering, smooth and elastic spheres in close contact. This energy of adhesion of both surfaces, $\Delta\gamma$, may be expressed as:

$$\Delta\gamma = \gamma_1 + \gamma_2 - \gamma_{12} \qquad (2-12)$$

where γ_i's are the excess surface free energies of surfaces 1 and 2 respectively and 12 the interface. The inclusion of the surface energies would mean that the apparent Hertz load P_1 acting between the two elastic bodies is bigger than the applied load P_0. The relationship between P_0 and P_1 is shown by

$$P_1 = P_0 + 3\Delta\gamma\pi R + \sqrt{6\pi\Delta\gamma R P_0 + (3\pi\Delta\gamma R)^2} \qquad (2-13)$$

The Hertz equation (2-9) modified to take into account the surface energy effect is

$$a^3 = \frac{R}{K}(P_0 + 3\Delta\gamma\pi R + \sqrt{6\pi\Delta\gamma R P_0 + (3\pi\Delta\gamma R)^2}) \qquad (2-14)$$

As the applied load P_0 is made negative, a limiting case will be obtained when the surfaces separate. For a real solution to equation (2-14),

$$6\pi\Delta\gamma R P_0 \le (3\pi\Delta\gamma R)^2 \qquad (2-15)$$

Thus the separation of spheres will just occur when

$$P_0 = P_C = -\frac{3}{2}\pi\Delta\gamma R \qquad (2-16)$$

and P_C is also known as the pull-off force [58, 59].

This model has been widely used for many adhesion force studies [48-50, 52, 59, 61], and the experimental data have shown that it is appropriate for highly deformable bodies, cases with high surface energies, cases where the contact radius is small compared to the particle radius and also for low elastic modulus.

2.3.3 DERJAGUIN, MULLER AND TOPOROV (DMT) THEORY

Like the JKR theory, the DMT theory [60] also assumes that there are attractive forces that act to deform spheres in contact. However in this theory, the attractive forces are acting outside the contact region. It also takes into account the work of molecular attraction in the circular zone of contact and assumes that the two surfaces in contact will part only when the contact area approaches zero.

It is summarized simply by one principal equation for the adhesion force with the contact radius and is given by

$$P_C = -2\pi\Delta\gamma R \qquad (2-17)$$

Unlike the JKR case, the DMT model is less favored by researchers. It was used by Burnham [62] for its applicability to small, hard bodies with low surface energies.

The JKR and DMT theories are not in conflict with each other but should be considered as the opposite ends of the same scale. The Maugis equation[63] is normally employed to determine which model should be used to best suit a particular situation.

On a molecular level the energy of adhesion per unit area, $\Delta\gamma$, between flat slabs can be modeled approximately with long range interactions using a Hamaker constant A_H:

$$\Delta\gamma = \frac{A_H}{12\pi D_0^2}, \qquad (2-18)$$

Where Do = 0.165 nm is the nominal value used for cut-off separation[42, 46].

2.3.4 MAUGIS EQUATION

In 1992, Maugis[63] highlighted differences in assumptions and predictions between the JKR and DMT theories. He suggested that the transition between these models can be predicted from the dimensionless parameter l defined by

$$\lambda = \frac{2.06}{z_0}\sqrt[3]{\frac{RW_A^{\ 2}}{\pi K^2}} \qquad (2-19)$$

Where z_0 is the equilibrium separation distance between the probe and the substrate, R the radius of the probe, WA is the work of adhesion, and K the reduced elastic modulus for the particle substrate system where

$$\frac{1}{K} = \frac{3}{4}\left(\frac{1-\upsilon_P^2}{E_P} + \frac{1-\upsilon_S^2}{E_S}\right) \qquad (2-20)$$

υ is the Poisson ratio and E is the Young's modulus, and p and s stand for probe (particle) and substrate respectively.

For $\lambda \rightarrow \infty$ ($\lambda \geq 5$) the JKR model applies whereas the DMT model is more appropriate for systems with $\lambda \rightarrow 0$ ($\lambda \leq 0.1$).

2.3.5 PARAMETRIC TIP – FORCE DISTANCE RELATION (PT/FDR)

Recognizing the need for a more geometrically appropriate model, Argento and French proposed a new parametric tip force – distance relation (PT/FDR) [64] for the long-range (non-contact) interaction of a typical AFM probe with a flat substrate. Their model AFM tip was composed of a cylindrical shaft, followed by a conical section, and terminated by a spherical cap. The non-retarded VDW interactions were assumed to be the only forces present. In the manner of Hamaker, the interaction between the model tip and flat surface was solved analytically, giving the force of interaction as a function of a Hamaker constant A_H, tip radius, and cone angle. The model is applied by fitting to our experimental data to determine the geometrical parameters and Hamaker constant. As shown in the chapters 3 and 4, their results suggest strongly that local curvature of a small tip radius (R < 100 nm) can cause significant deviations from conventional sphere-plane and sphere-sphere Hamaker VDW models.

2.3.6 SQUARE PYRAMID AFM PROBE AND A FLAT SAMPLE SURFACE (SPFS) MODEL

Consider the model shown in Figure 2-4 below.

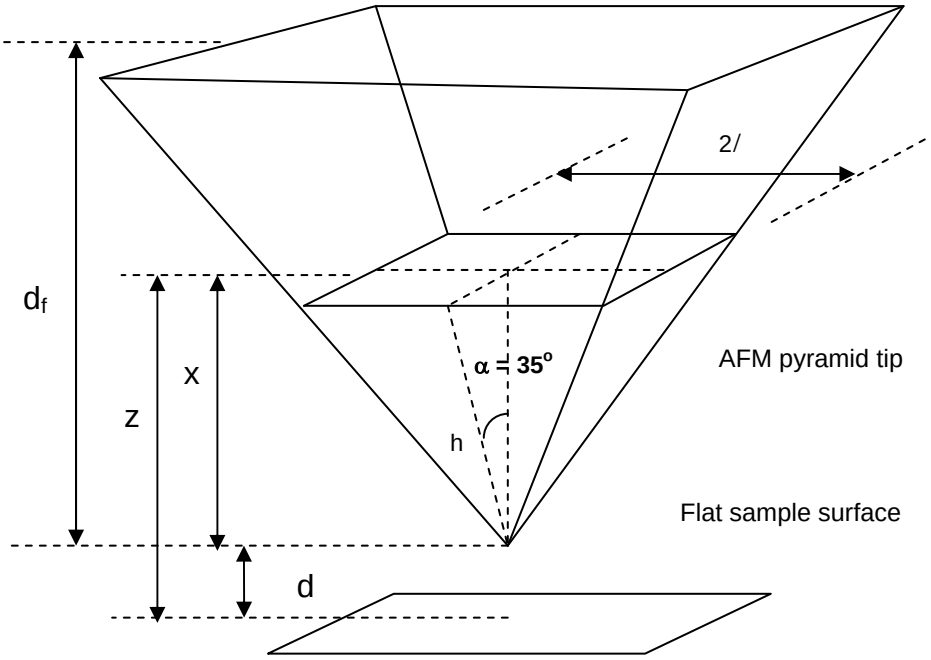

Figure 2 – 4 . Square pyramid-flat surface (SPFS) model. 2*l* is the base length of the penetration depth of the pyramid part of the tip, x the penetration depth, h the hypotenuse, d the probe-sample separation and α is the acute angle of the pyramid.

The cross sectional area of the pyramid part in contact with the surface (penetration depth) is

$$a_{cross} = 4x^2 \tan^2 \alpha \,, \qquad (2-21)$$

while the tetrahedron face area is

$$a_{tet} = 4x^2 \frac{\sin \alpha}{\cos^2 \alpha}. \qquad (2-22)$$

We next derive the total energy potential, Φ(z) for a pyramid-slab interaction as a function of the distance of their separation *z*. This is given by

$$\Phi(z) = -\int_d^\infty \left(\frac{\rho N_A \pi}{M}\right)^2 \frac{\beta}{6\pi z^3}\left(4x^2 \tan^2\alpha\right)dz\,, \qquad (2-23)$$

where ρ is the density, N_A the Avogadro's number, M the molecular weight of the material of the square pyramid and β a molecular interaction constant. Rearranging,

$$\Phi(z) = -\left(\frac{2\tan^2\alpha A_{slab}}{3\pi}\right)\int_d^\infty \frac{x^2}{z^3}dz \qquad (2-24)$$

and substituting $x = z - d$, $\delta = (2\,A_{slab}\tan^2\alpha)/3\pi$ and $A_{slab} = \beta(\rho\ \mathrm{N_A}\pi\ /M)^2$, with A_{slab} being the Hamaker constant for a purely slab-slab interaction (but noting that this is not chemically identifying A_{slab} as the slab material), we have

$$\Phi(z) = -\delta\int_d^\infty \frac{(z-d)^2}{z^3}dz\,. \qquad (2-25)$$

Setting the upper dimension of the integration limit as d_f, $\Phi(z)$ is reduced to

$$\Phi(z) = -\delta\left[\ln\left(\frac{df}{d}\right) + \frac{2d}{df} - \frac{d^2}{2df^2} - 1.5\right] \qquad (2-26)$$

We consider d_f as an arbitrarily chosen distance beyond which the van der Waals interaction becomes insignificant[42].

The work of adhesion ($\Delta\gamma$) of the pyramidal tip in close contact with the planar surface is derived in the same way, but by including in the integral the 'contact area' of the pyramid surface at the 'depth' of interaction, x

$$\Delta\gamma = -\int_d^\infty \left(\frac{\rho N_A \pi}{M}\right)^2 \frac{\beta}{6\pi z^3}\left(4x^2 \tan^2\alpha\right)\left(\frac{\cos^2\alpha}{4x^2\sin\alpha}\right)dz\,, \qquad (2-27)$$

After rearrangement and simplification, we have

$$\Delta\gamma = -\frac{A_{slab}}{6\pi}\sin\alpha\cos\alpha\int_{d}^{\infty}\frac{1}{z^3}dz\,, \qquad (2-28)$$

Integrating and substituting in the limits, we get

$$\Delta\gamma = -\frac{A_{slab}}{12\pi d^2}\sin\alpha\cos\alpha\,. \qquad (2-29)$$

(2-29) is different than the energy of adhesion described earlier in equation 2-18 for both the FDR and DMT models since it incorporates a shape factor of ($sin\ \alpha\, cos\ \alpha$) that accounts for the pyramidal-slab geometry, as opposed to two elastic spheres. Now, the work of adhesion $\Delta\gamma$ is equivalent to the work W required to pull off the tip from the surface (area under the force-distance graph) per unit area of interaction. Mathematically, this is expressed as

$$\Delta\gamma = \frac{W}{Area} = \frac{W}{\left(4x^2\,\frac{\sin\alpha}{\cos^2\alpha}\right)} = -\frac{A_{slab}}{12\pi d^2}\sin\alpha\cos\alpha \qquad (2-30)$$

Rearranging, we obtain

$$x = \sqrt{-\frac{3\pi W d^2 \cos\alpha}{A_{slab} \sin^2 \alpha}} \qquad (2-31)$$

for the "penetration depth" of interaction at the tip. Here the "penetration depth" is a parameter describing the effective depth of van der Waals (VDW) forces. In this case d is set as 0.165nm, the nominal cut-off distance of separation for two surfaces on contact. The effective tip radius at depth x, r_e, is taken from a hemispherical-cap approximation to the square pyramidal penetration volume, and can be calculated from $2\pi r_e^3/3 = 4l^2x$, where $l = x \tan \alpha$ (See Figure 2 – 4).

CHAPTER III

MEASUREMENT OF POLYAMIDE AND POLYSTYRENE ADHESION WITH COATED-TIP AFM

Atomic Force Microscopy was used to measure the adhesion forces between polyamides, polystyrene and AFM tips coated with the same materials. The polymers employed were polyamide 6 (PA6), PA66, PA12 and polystyrene (PS). All adhesion forces between the various unmodified or modified AFM tips and the polymer surfaces were in the range -1.5 nN to -8 nN. The weakest force was observed for an unmodified AFM tip with a PS surface and the strongest was between a PS-coated tip and PS surface. The results point to both the benefits and drawbacks of coated-tip AFM force-distance measurements. We observe that adhesion forces between the two most dissimilar (polar vs. nonpolar) materials were significantly different depending on their relative placement on the AFM tip or substrate. On the other hand adhesion forces between more similar materials are symmetric. The contact radii were computed via two contact mechanics models: Derjaguin, Muller, and Toporov (DMT) and Johnson, Kendall, and Roberts (JKR); and two non-contact adhesion models: parametric tip – force distance relation (PT/FDR) and a square-pyramid-flat-surface (SPFS) model developed herein. In our study, estimates from three adhesion models (the JKR, DMT and PT/FDR) gave work of adhesion and radii of contact that were two orders of magnitude smaller than experimental approach curve measurements, while the SPFS model produced values 10

times smaller, and is a closer representation of the geometry between the AFM tip and the flat surface.

3.1 EXPERIMENTAL MATERIALS AND METHODS

3.1.1 POLYMER FILM SAMPLES AND PREPARATION

A series of thin polymer films was prepared on Piranha-etched silicon substrates[65]. These consisted of polystyrene, PS (average molecular mass = 100,000, Avocado Research Chemicals, Lancashire, England), polyamide 6 (PA6, average molecular mass = 10,000, Aldrich Chemical Co., Inc., Milwaukee, WI), PA66 (average molecular mass = 22,000, Aldrich Chemical Co., Inc., Milwaukee, WI), and PA12 (average molecular mass = 40,000, Arkema Group, Philadelphia, PA). PA12 is included in this study to investigate the effect of amide bond spacing on force interactions. The structures of PA6 and PA66 are shown in Figure 1-2. Compared to the PA6 and PA66, PA12 has its amide linkages spaced twice as far apart, and is significantly more flexible and hydrophobic. The PS solution was prepared by dissolving 10% by mass in toluene while 1% by mass PA6, PA66 and PA12 solutions were prepared in hexafluoroisopropanol (HFIP, TCI America, Portland, OR). Polymer films were made by a knife-edge coating technique described in detail elsewhere [66, 67]. Films were dried at 80 °C under vacuum for 2 hours to remove any remaining solvent. Detailed measurements of film thicknesses are not reported here; however, it was verified that film

thickness exceeded 1 μm, which is far greater than the range of van der Waals interactions (10 nm) being probed here.

3.1.2 AFM PROBES AND THEIR MODIFICATION

The AFM used was a Thermomicroscopes™ Explorer (Veeco Metrology Inc., Santa Barbara, CA) employing V-shaped silicon nitride cantilevers of spring constant 0.10 N/m. The scanner has a vertical range of 1 μm. A micropipette attached to a micromanipulator was used in conjunction with a microscope (magnification 20x) to coat the polymers onto the AFM tip (cantilever apex). The micropipette containing a dilute polymer solution (~1 wt %) was brought into contact with the AFM tip and the probe tip was coated with the polymer via capillary action. The same tip was used to measure all interactions within a given polymer series, to ensure that the spring constant and tip radius were kept constant between the different substrates. Force measurements were made between the AFM tips (unmodified and modified) and different surfaces (PA6, PA66, PS and Si). For each set of tip-surface measurements, 20 force-distance measurements were taken from two separate Si wafers within three randomly-chosen 10 μm by 10 μm areas on each surface. To investigate whether surface roughness is a factor in the adhesion measurements, we used the AFM to determine the root-mean-square and mean roughness of each surface-coating. For each of three 10 μm x 10 μm scans, the image was split into 4 sectors for a total of 12 roughness measurements.

3.1.3 CONTROL OF HUMIDITY

For AFM force measurements in air, humidity and grounding of the sample surface influence the dissipation of static electrical charges. In addition, high humidity (> 60%) causes capillary condensation between the tip and surface, interfering with the measurement.[68] The AFM was enclosed in a humidity-controlled acrylic chamber at 40% relative humidity (RH).

3.1.4 SCANNING ELECTRON MICROSCOPY (SEM)

SEM (Hitachi Model S-800) was used to confirm that the modified tips were coated with the respective polymers. This was done after the force measurements were completed. The tips were mounted on metal stubs using carbon tape and sputter-coated with gold before imaging using an accelerating voltage of 10 kV.

3.2 RESULTS AND DISCUSSION

A typical force distance curve obtained for a single measurement of a PA6 coated AFM tip against a PA6 polymer surface is shown below in Figure 3-1. There is difficulty in establishing the true 'set-point zero' for the point of contact of the AFM probe with the surface. Many researchers have defined the point of contact by using a 'geometric' approach: the point of contact is taken as the intersection of the baseline and the gradient of the approach curve [69]. With this in mind, an approximation of the contact radius can be found by using the penetration depth (that is, distance the probe moves into the surface

beyond the zero set point) and the acute angle from the base of the pyramidal AFM probe as shown in Figure 2 – 4.

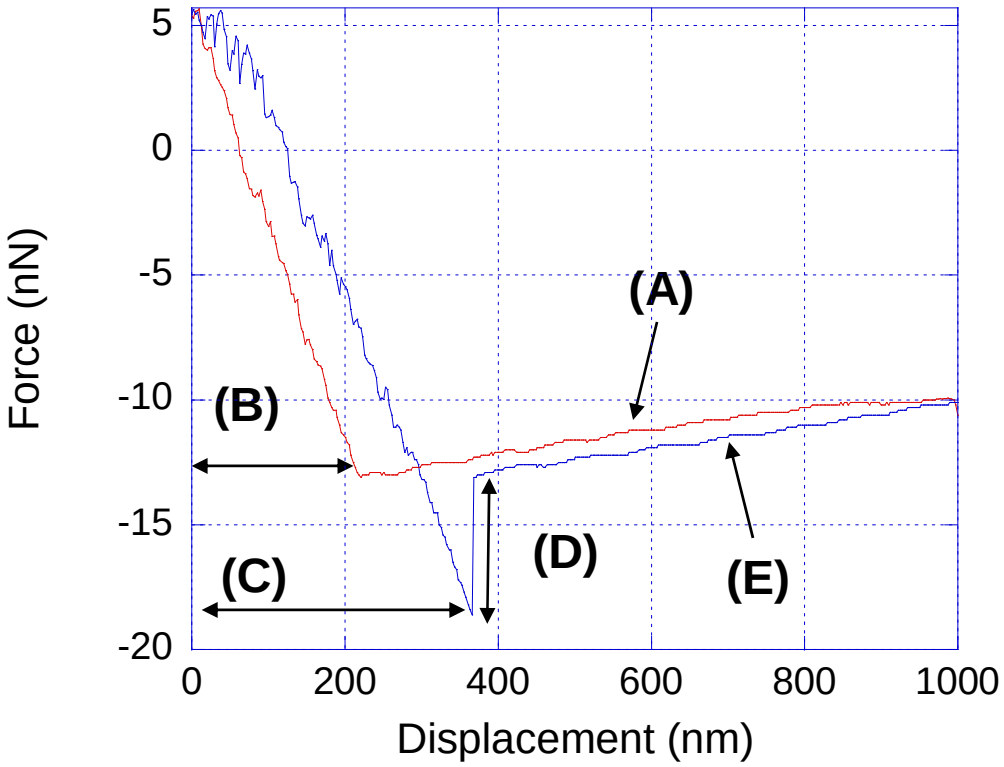

Figure 3 – 1. Raw force distance curve recorded by the AFM for a PA6-coated tip interaction with PA6 film on Si. (A) the initial approach, (B) the "penetration" depth using the geometric technique [69], (C) the pull-off distance at which cantilever snaps off the surface to a point where there is no net attractive or repulsive force between the tip and sample surface. (D) the strength of the adhesive force between tip and sample. (E) the retraction curve.

This gives a contact radius, r_e, of 153 nm, based upon an observed penetration depth of x = 218 nm from Fig 3-1, where r_e is the effective radius of circle with area equal to the cross-section of the square-pyramid tip at that penetration depth (See Section 2.3.6). An alternative method is to compute contact radius and penetration depth from

the force data using the adhesion models. These values are compared to the geometrical approach below in the "Modeling of Force Data" section. The adhesive force was 5.4 nN and pull off distance of 366 nm was for the data in Figure 3 – 1.

Two artifacts are visible in the force-distance curve: the 'reverse path' effect[70, 71] and the oscillation of the non-contact line[70, 72]. In the reverse-path effect, the retraction curve lies above the approach curve. This is not a physically-realistic result, as forces exerted by the sample on the tip during unloading should be less than (plastic) or equal (elastic) to those exerted upon loading. Possible reasons for this phenomenon include piezoactuator hysteresis[72] and friction induced forward bowing of the AFM cantilever[71] as the sample is approached. The oscillation and slope of the non-contact line is due to interference between reflections off the sample surface and the upper face of the cantilever. Neither of these artifacts alter significantly (within the experimentally observed error) the value of attractive forces measured from the pull-off (retraction). However, these artifacts present more difficulty when calculating mechanical properties, such as elastic modulus of the sample, from the approach curve, a topic not covered in this study.[72]

The highest load applied in our study was 35 nN and the typical load was 18 nN (Figure 3-1) at the point of maximum deflection. Using a tetrahedral face contact area of 5140 nm2 (based on an effective tip contact radius of 30 nm), the maximum and typical stresses were 6.8 and 3.5 MPa, respectively. The softest material in our study was PA12, with a reported modulus of 1400 MPa and yield stress of 73 MPa. It is clear that the

maximum applied load is insufficient to induce permanent deformation. In addition, the maximum elastic (recoverable) deformation is very small at 6.8/1400 x 100% = 0.5% strain.

3.2.1 POLYMER - POLYMER INTERACTIONS

Force data for some of the different tip and surface combinations are presented in Table 3-1, and Figure 3-2 illustrates the respective pull – off distances. For the unmodified Si_3N_4 tip, the strongest adhesion force occurs with an uncoated silicon wafer, while the weakest is for the interaction between the tip and a polystyrene (PS) surface. There is no significant difference between the three polyamide interactions with the unmodified tip.

Table 3 – 1. Adhesion force, nN, ± 95% confidence interval for tip – polymer surface interactions.

	AFM Tip Coating				
Surface	Si_3N_4	PA6	PA66	PA12	PS
PA6	2.8 ± 0.3	4.2 ± 0.6	3.3 ± 0.3	4.3 ± 0.4	6.3 ± 0.5
PA66	2.6 ± 0.2	2.6 ± 0.4	-*	2.6 ± 0.3	5.6 ± 0.8
PA12	2.3 ± 0.2	3.8 ± 0.7	3.4 ± 0.4	-*	3.0 ± 0.4
PS	1.5 ± 0.03	3.5 ± 0.2	2.4 ± 0.1	2.5 ± 0.1	8.0 ± 0.3
Si	5.5 ± 0.5	6.0 ± 0.6	5.0 ± 0.4	2.6 ± 0.2	2.9 ± 0.1

*(Force data for PA66 - PA66 and PA12 – PA12 interactions could not be obtained reliably.)

These forces follow the trends expected based on chemical structure and known Hamaker constants. The similar chemistry between the AFM tip and the silicon wafer apparently results in that pair having the strongest attraction all those involving the Si_3N_4 tip. Metal oxides and nitrides typically have higher Hamaker constants than organics[42]. The polar groups in the polyamides likely enable dipole-dipole interactions with the tip, although these are apparently weaker than the Si_3N_4-SiO_2/Si interactions. Polystyrene interacts primarily via dispersion (London) forces, and as a result it is not surprising the PS interaction with the Si_3N_4 tip is the weakest.

The PA6 tip coating experienced its greatest adhesion force with the silicon wafer followed in decreasing order by the PA6 surface, the PA12, PS and PA66. Among these polymers, the error bars (95% confidence) all overlap. Additional surface forces other than van der Waals, such as hydrogen bonding interactions (C=O: + :O-H or N-H + :O-H), are likely to contribute to these differences in adhesion force. The data for the PA66 coated tip was consistent with PA6, where the adhesion with the SiO_x/Si surface was strongest.

In contrast with the other polyamides, the PA12-coated tip adhered strongest with PA6. Apparently, the reduced number of amide bonds per segment does not allow for strong interactions with SiO_2/Si as in the case of PA6 and PA66. In fact, PA12-SiO_2/Si forces were about the same as PS-SiO_2/Si. The PA12-PA6 force was about 40% higher than PA12 and the other surfaces. This could be due to the higher molecular flexibility of PA6 (compared to PA66), allowing chain rearrangements for optimizing interactions with

about half the number of the polyamide bonds per segment on the PA12. T_g values for PA12, PA6 and PA66 are 29, 56 and 82 ^oC,[73] respectively. Force data between the PA12 – coated tip and other surfaces were not significantly different from each other.

The polystyrene (PS) coated tip had unexpectedly large adhesion forces with the PA6 and PA66 surfaces. This was not the case for the reverse situation of PA6- and PA66-coated tips interacting with the PS surface, which were approximately 45% and 58% lower, respectively. Figure 3-2 shows the adhesion force differences between various tip surface combinations.

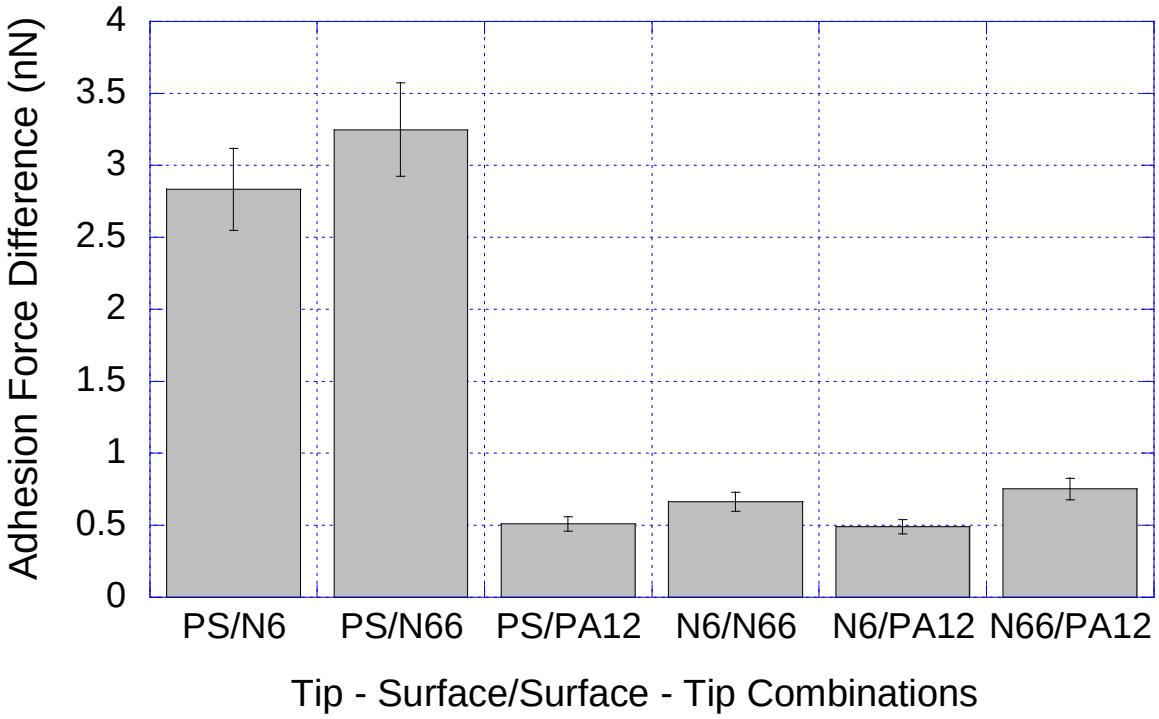

Figure 3 – 2. Bar graph of the difference in adhesion force between the two configurations for each tip – surface pair. PS/PA6 refers to the difference between the force when tip = PS and surface = PA6 minus the force for tip = PA6 and surface = PS.

In fact, none of the "mixed" tip-surface interactions exactly match those with the chemistry reversed in Figure 3. This suggests the presence of factors that contribute to the interactions other than material chemistry. Possibilities include capillary effects, surface morphology, and sample geometry. With relative humidity during the measurements kept constant at around 40 – 45%, capillary forces could play a role if water condensed between the tip and surface at close contact *only* when *polyamide* is the surface coating, since the force is *always more attractive when a polyamide is the surface coating*. Many researchers have studied the relationship between AFM adhesion force and ambient relative humidity on different surfaces. For the case of mica, there is disagreement concerning the dependence of adhesion on relative humidity (RH) [74]. Some work suggested that adhesion induced by humidity effect peaked as low as 25 – 30% RH [75], while others showed this at RH ~ 80% [76]. To estimate the possible effect of condensation in our experiments, we apply the Kelvin equation [42],

$$r_K = \frac{\gamma V}{RT \log\left(\frac{p}{p_{sat}}\right)} \qquad (3-1)$$

where r_K is the Kelvin radius and V the molar volume ($\gamma V/RT$ = 0.54 nm for water at 20^{o}C). The formation of a spherical convex water meniscus of radius about 1.56 nm is predicted at p/p_{sat} = 0.45. Setting $\gamma = \gamma_{water\text{-}air}$ = 73 dynes/cm, a force of about -1 nN is predicted. This suggests that humidity may explain the small (< 1 nN) differences in

PS/PA12, PA6/PA66, PA6/PA12 and PA66/PA12. However, the average roughness, *Ra*, is much higher than the minimum radius of curvature for condensation (1.5 nm). *Ra* is 70 nm on PA6 and 120 nm on PA66.

Even if capillary condensation were occurring, that effect alone is only of a magnitude that explains the force differences between the most chemically similar tip-surface combinations, e.g., the polyamide-polyamide and PS-PA12 interactions. (PA12 is considerably more hydrophobic than PA6 or PA66). The most dissimilar tip-surface combinations, PS-PA6 and PS-PA66, show force differences in Fig. 3 that are at least *three times larger* than the other tip-surface combinations. We suggest that these large differences are related to the geometrical asymmetry between the tip (pyramid) and surface (plane). This geometrical asymmetry may 'amplify' the polarity differences between PS and the PA6 or PA66. The Hamaker model, commonly used to interpret colloidal interactions, is based on an integration of all binary van der Waals interactions between the tip and surface atoms. Even for geometrically dissimilar objects and accounting for all three types of dipole and induced dipole VDW interactions, a binary-additive integration yields identical results for both the PS(tip)-PA6(surface) and PA6(tip)-PS(surface) forces. However, the binary additivity assumption almost certainly breaks down in the case of a non-polar substance interacting with a polar one across a geometrically-asymmetrical interface. PS and polyamides (PA) both contribute dispersion (London) forces, whereas the dipoles in PA can induce dipoles in PS at close approach, e.g. tip and surface within 10 nm. However, the collective effects of the surrounding dipoles on any given PA dipole, as well as the shape of the electric field they

generate, will be a function of the tip shape. Placing molecules with a permanent dipole on the bottom surface creates a uniform electric field. In contrast, if the permanent dipoles (PA6 or PA66) were placed on the 35° AFM tip, the induced electric field would have a different magnitude and direction. In addition, only a small portion of the tip falls within 10 nm of the surface (the effective interaction distance). Ordering of PA at the air or AFM tip interfaces could make this geometric dependence even stronger. When PA is coated on the bottom surface (and PS on the tip), one expects a larger electric field acting to induce dipoles in a smaller number of PS molecules. In the opposite situation, PA(tip)-PS(surface), a smaller electric field will act on a larger number of PS molecules. The force hysteresis observed in Fig 3-2 follows this reasoning, e.g., the PS(tip)-PA(surface) force is larger than the PA(tip)-PS(surface).

Other potential causes of the discrepancies in Fig. 3 include differences in morphology and crystallinity between the coatings on the AFM tip versus the flat substrate surface. Surface roughness, an indicator of morphology, can have a strong effect on adhesion [45, 77]. SEM images of the various modified AFM tips after repeated force measurements are shown in Figure 3-3. Our intention was to observe the condition of the tips looking for evidence of tears, cracks, or defects in the coating, or the accumulation of dust. The electron micrographs do not indicate any such defects. While they do not provide direct evidence of a successful coating at the apex, neither do they suggest the coating was ineffective. They show that the modified AFM probes were coated with polymer, although the distribution of thickness was difficult to control. Van der Waals interactions are known to be dominated by the atoms in the first ~10 nm, and

the effect of atoms deeper than 10 nm is negligible.[42] Figure 3-3 indicates that coatings are visibly thicker than 10 nm, although the absolute thickness cannot be determined in this manner.

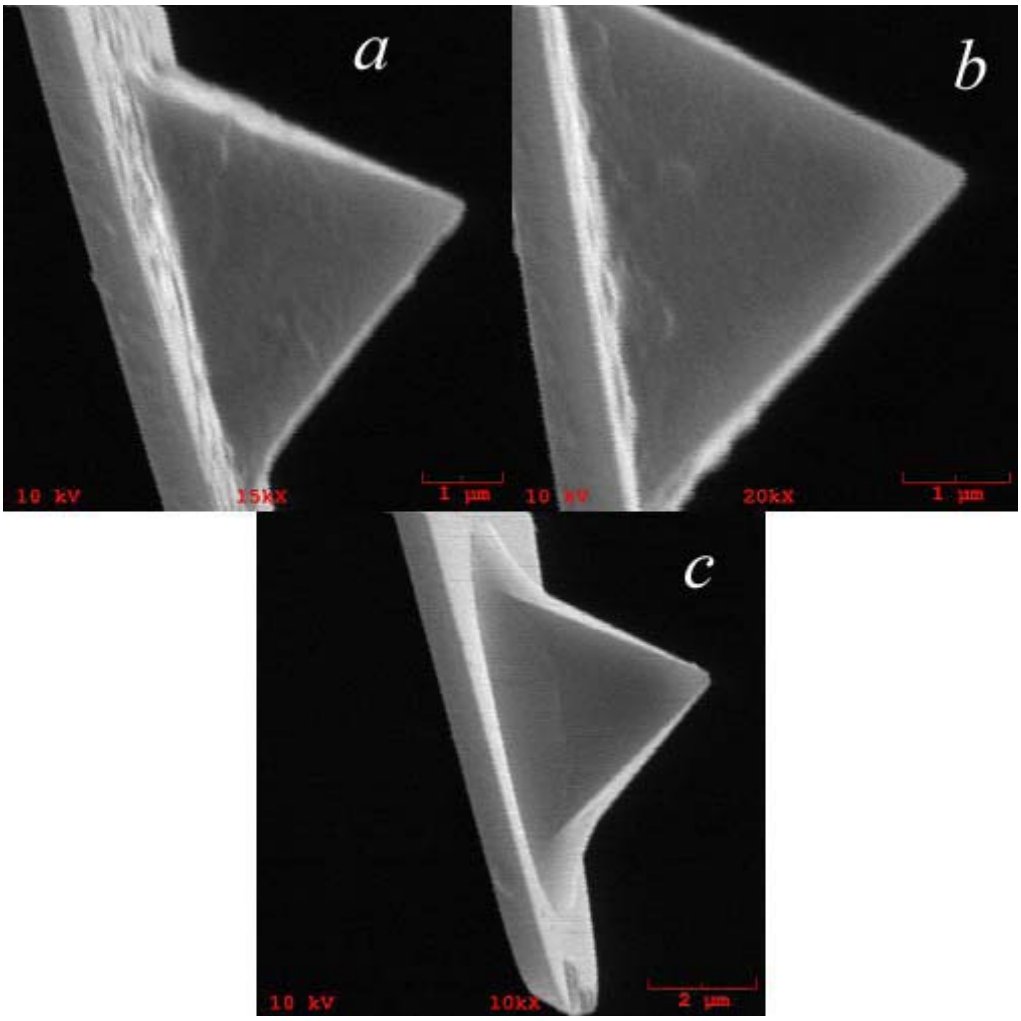

Figure 3 – 3. SEM images of coated AFM tips. (a) PA6, (b) PA66, (c) PS. Scale bars are 2 µm (c) and 1µm (a, b).

The SEMs indicate that the PA6, PA66 (Fig 3-3a and 3-3b) and PA-12 (not shown) tip coatings are rougher than the PS (4c) coatings, consistent with surface roughnesses measured on flat surfaces. Table 3-2 presents *Ra* (arithmetic average height) and RMS (root mean square deviation of surface profile from *Ra*).

Table 3 – 2. Surface roughness of the various polymeric surfaces. Uncertainty is ± 95% confidence interval.

Surface	PA6	PA66	PA 12	PS	Si
Ra (nm)	70.1 ± 21.5	124.1 ± 27.5	93.4 ± 9.9	6.6 ± 0.5	0.2 ± 0.2
RMS (nm)	84.8 ± 21.5	150.7 ± 29.8	115.8 ± 11.5	7.8 ± 0.8	0.3 ± 0.2

The rougher surfaces, e.g., the polyamides, displayed stronger mixed-chemistry adhesion forces in Figure 3-2 compared to when the surface coating was either PS or Si. However the PA66 surface, which is the roughest of all, produced adhesion forces which are statistically indistinguishable from the other polyamide surfaces. Polystyrene (PS) has the smoothest coated surface, but self-adhesion forces with a PS-coated tip are larger than the PS tip's interaction with *any* other surface. This suggests that while surface roughness cannot be excluded as a factor determining tip-surface force hysteresis, it is probably not the primary influence. Rather, the hysteresis seems to stem primarily from chemical differences between the tip and surface coatings.

We are unaware of any microscopic or spectroscopic methods to unambiguously confirm the presence of a specific surface chemistry in the nanoscale region of the tip apex. There have been hundreds of studies performed with chemically-modified AFM tips[78-81], and a survey of this literature indicates that the change in measured forces on a

control surface is the standard method used to infer successful modification of the tip. Therefore, our approach in this work was to perform a large number of control measurements using substrates coated with the *same materials as those applied to the modified tips*. The resulting matrix of interactions (Table 3 – 1) allows one to compare the like- and unlike- interactions between all of the modified and unmodified tips and surfaces. If deposition of the polymers took place *only at the base of the tip* and not the apex, then there should be no difference in force measurements between the modified versus unmodified tip/surface combinations. But we have observed forces that are consistent with successful apex modification. We found two exceptions involving the most dissimilar coatings (PS-PA6 and PS-PA66) and these were pointed out in Figure 3 – 2. It is possible that this discrepancy between the coated-tip versus coated-surface measurement is due to incomplete coating on the apex, among other possible issues.

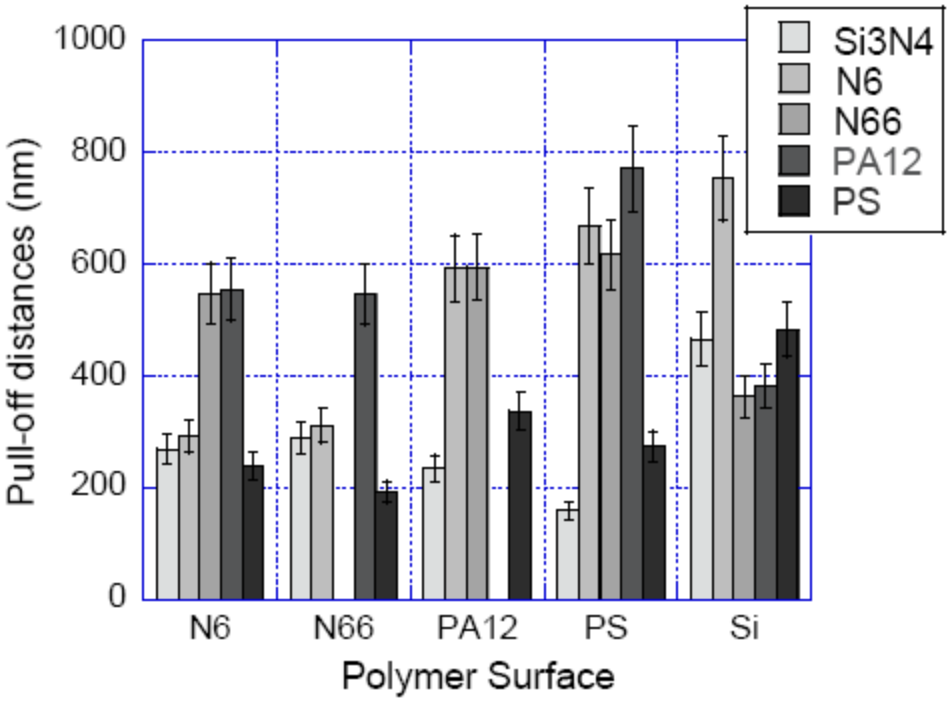

Figure 3 – 4. Pull-off distances at ±95% confidence intervals for various tip surface interactions.

Figure 3 – 4 shows pull-off distances associated with each of the force measurements discussed above. For the unmodified tip, the trends in adhesion force were similar to trends among the pull-off distances. The weakest interaction, Si_3N_4 tip with PS surface, was evident also as the shortest pull-off distance. At about 450 nm, the silicon wafer surface had the longest pull-off distance with the Si_3N_4 tip, corresponding with that being the strongest force.

However, the pull-off distances (Fig. 3 – 4) did not correlate with the adhesion force data for most of the coated-tip / surface interactions. This discrepancy could be due to factors discussed above concerning the tip-surface force differences. The PA6 – coated tip had longer than expected pull-off distances with the PA12, PS and silicon surfaces, compared to the PA6 and PA66 surfaces. The pull-off distances were greater than those of the unmodified tip, consistent with the adhesion force data shown in Table 3 – 1. PA66- and PA12-coated tips had relatively long pull-off distances that were not correlated with their moderate adhesion forces. The polystyrene coated tip had relatively short pull-off distances compared to the others.

3.2.2 MODELING OF FORCE DATA

Here, we compared the performance of four adhesion models in representing the measurements presented above. First, we used the values of ε and η in Table 3 – 3, with Israelachvili's simplification[42] of the Lifshitz theory, to estimate $A_{tip\text{-}air\text{-}surface}$ (Eq. 2 – 5) and work of adhesion $\Delta\gamma$ (Eq. 2 – 18). Then $\Delta\gamma$ and the measured forces were used to calculate the radii of contact via the JKR, DMT, and PT/FDR. The contact radius from

the SPSF model was calculated from Eq. 2 – 30 by first determining the adhesion work (W) from the experimental force-distance curves, which is the triangular area bounded by the approach and retraction lines at the pull-off point. The tetrahedron area (a_{tet}) of the tip facing the plane was then computed by equating the right hand side of (Eq. 2-30) with (W/a_{tet}). The tip radius l is determined from a_{tet} using (Eqs. 2-22) and $l = x\tan\alpha$.

Table 3 – 3. Relevant physical constants for the polymers, substrates and tips. (T = 298K)

Material	ε (at 1 MHz)	η
PS[a]	2.5	1.6
PA6[a]	3.5	1.5
PA66[a]	3.6	1.5
PA12[a]	4	1.5[b]
Si	11.7[c]	3.9[d]
SiO_2	3.9[e]	1.5[e]
Si_3N_4 (AFM tip)	7.5[e]	2.1[e]

a – See Ref.[73]; b – Estimated; c – See Ref. [82]; d – See Ref.[83]; e – See Ref.[84].

The computed contact radii are compared to radii estimated from the experimental approach curves, $R_{Approach}$. For the non-contact models, PT/FDR and SPFS, we use the term contact radius to mean the AFM tip radius. The results are tabulated in Table 3-4.

Table 3 – 4. Average contact radii (nm) derived from adhesion models of experimental forces (R_{JKR}, R_{DMT}, $R_{PT/FDR}$, R_{SPFS}) and from experimental approach curves ($R_{Approach}$). Most error bars are within +/- 10% of the mean value.

Surface	AFM Tip	A (J x 10^{20})[a]	R_{JKR} (nm)	R_{DMT} (nm)	$R_{PT/FDR}$ (nm)	$R_{Approach}$ (nm)	R_{SPFS} (nm)
PA6	Si_3N_4	13.3	4.6	3.5	3.6	126	17.2
PA6	PA6	7.9	11.7	8.8	9.0	136	27.6
PA6	PA66	7.9	9.1	6.9	7.0	256	34.1
PA6	PA12	7.9	11.9	8.9	9.1	259	39.2
PA6	PS	8.6	16.1	12.1	12.2	112	30.2
PA66	Si_3N_4	13.3	4.3	3.2	3.4	135	17.2
PA66	PA6	7.9	7.3	5.5	5.6	146	22.5
PA66	PA12	7.9	7.3	5.5	5.6	255	30.4
PA66	PS	8.6	14.3	10.8	10.9	88	25.4
PA12	Si_3N_4	13.3	3.8	2.8	3.0	110	14.6
PA12	PA6	7.9	10.5	7.9	8.1	277	36.6
PA12	PA66	7.9	9.4	7.0	7.2	278	35.7
PA12	PS	8.6	7.5	5.7	5.8	157	24.2
PS	Si_3N_4	14.6	2.2	1.7	1.8	74	9.6
PS	PA6	8.6	8.9	6.7	6.8	312	37.5
PS	PA66	8.6	6.1	4.6	4.7	288	29.5
PS	PA12	8.6	6.2	4.7	4.8	360	33.4
PS	PS	9.4	18.6	13.9	14	128	34.8
Si*	Si_3N_4	41.5	2.9	2.2	2.3	218	18.8

Table 3 – 4 (continued)

Surface	AFM Tip	A (J x 10^{20})[a]	R_{JKR} (nm)	R_{DMT} (nm)	$R_{PT/FDR}$ (nm)	$R_{Approach}$ (nm)	R_{SPFS} (nm)
Si*	PA6	23.4	5.7	4.2	4.4	352	31.8
Si*	PA66	23.4	4.6	3.5	3.0	169	19.8
Si*	PA12	23.4	2.4	1.8	2.0	179	14.6
Si*	PS	25.7	2.5	1.8	2.0	226	16.8

[a]Hamaker constants, $A = A_{tip\text{-}air\text{-}surface}$, were calculated using Lifshitz theory with constants in Table 3.

The contact radii (in Table 3 – 4) calculated using the experimental approach curves ($R_{Approach}$) are always about 1 magnitude higher than those calculated using the JKR, DMT, PT/FDR and SPFS theories. The JKR, DMT, and PT/FDR models yield the lowest contact radii estimates, but are all three similar in magnitude falling in the range 2 to 18 nm. These values are slightly smaller than radii commonly reported in previous studies, e.g., ~20 - 50 nm[46, 85]. The contact radii predicted from the SPFS theory are intermediate between the $R_{Approach}$ values and the JKR, DMT, and PT/FDR models. Values of R_{SPFS} fall in a range that is generally reported for tip-radii in AFM force-distance measurements, e.g., ~20 - 50 nm[46, 85].

It is likely that the contact radii from the experimental approach curves are overestimated for the AFM measurements presented here, for reasons discussed above (see Figure 3-1).

Maugis[63] had suggested that a dimensionless parameter λ be used to determine whether the JKR or the DMT model is appropriate for the system under study. He opined that for $\lambda \to \infty$ ($\lambda \geq 5$) the JKR model applies while the DMT model is more suitable for systems with $\lambda \to 0$ ($\lambda \leq 0.1$). For comparison purposes, we have included in Table 5 the Maugis numbers using the contact radii calculated from the JKR, DMT, Approach curve and SPFS models. The PT/FDR model is excluded as it does not use a straightforward work of adhesion parameter in its calculations. The Maugis numbers calculated from the 4 models were all in the range of 4 x 10^{-15} to 4 x 10^{-18}, indicating that the DMT model would be preferable. However we included JKR for a complete comparison, since this model is very commonly used in the literature.

Table 3 – 5. Maugis number, λ, derived from the AFM tip contact radii calculated via the JKR, DMT, Approach curve and SPFS models.

Surface	**AFM Tip**	λ_{JKR} **(10^{-18})**	λ_{DMT} **(10^{-18})**	$\lambda_{Approach}$ **(10^{-15})**	λ_{SPFS} **(10^{-18})**
PA6	PA6	2.0	1.9	4.6	2.7
PA6	PA66	1.8	1.7	5.5	2.8
PA6	PA12	2.8	2.5	7.7	4.1
PA6	PS	2.3	2.1	4.5	2.9
PA66	PA6	1.7	2.5	4.6	2.5
PA66	PA12	2.3	2.1	7.5	3.7
PA66	PS	2.2	2.0	4.0	2.6
PA12	PA6	2.7	2.4	7.9	4.0
PA12	PA66	2.5	2.3	7.8	3.9

Table 3 – 5 (continued)

Surface	AFM Tip	λ_{JKR} (10^{-18})	λ_{DMT} (10^{-18})	$\lambda_{Approach}$ (10^{-15})	λ_{SPFS} (10^{-18})
PA12	PS	2.5	2.3	6.8	3.7
PS	PA6	1.9	1.7	6.2	3.1
PS	PA66	1.6	1.5	5.9	2.7
PS	PA12	2.3	2.1	8.9	4.0
PS	PS	2.5	2.3	4.8	3.1

Table 3 – 6 shows Hamaker values obtained by substituting experimentally determined $R_{Approach}$ and forces into the DMT model. The average Hamaker values computed using this method are an order of magnitude smaller than is reasonable, (comparing to experiments and Lifshitz's theory for these materials). Since these Hamaker values are clearly underestimated using $R_{Approach}$, this contact radius not used further in our calculations.

Table 3 – 6. Average Hamaker constants, J x 10^{21}, derived from contact radii using the experimental approach curves' method and assuming DMT model.

	AFM Tip Coating				
Surface	Si_3N_4	PA6	PA66	PA12	PS
PA6	3.69	3.95	2.74	3.98	9.23
PA66	3.18	6.33	-*	1.49	10.28
PA12	5.03	0.88	2.06	-*	3.08
PS	5.39	2.89	3.44	2.24	10.2
Si	2.18	2.82	4.76	2.38	2.1

*(Hamaker constants were not available as force data for PA66 - PA66 and PA12 – PA12 interactions could not be obtained reliably.)

Of the four models investigated here, the SPFS model yielded the most reasonable estimates of tip radii. Here we demonstrate one avenue for using SPFS to calculate Hamaker constants. Our approach was to use the R_{SPFS} determined from a well-known 'reference' Hamaker value (PS-PS interaction in air), and assume this R_{SPFS} is a constant for the other measurements. The value of the PS-PS Hamaker constant used for our calculations was 7.35 x 10^{-20} J[86, 87]. This resulted in a 'reference' R_{SPFS} of 34.8 nm. By using this reference R_{SPFS} in (Eq. 2-30) together with the integrated experimental force-distance data (W), we obtained Hamaker constants, A, of the different tip-surface interactions. The results are shown in Table 3-7 and are of a magnitude close to that predicted by the Lifshitz theory.

Table 3 – 7. Comparison of average Hamaker constants, J x 10^{20}, calculated using the SPFS model based on PS-PS Hamaker value obtained from Israelachvili's simplified Lifshitz theory.

	AFM Tip Coating				
Surface	Si_3N_4	PA6	PA66	PA12	PS
PA6	5.65	8.46	12.9	17.2	11.1
PA66	5.49	5.84	-*	10.4	8.16
PA12	3.92	1.52	1.49	-*	7.18
PS	1.8	16.7	10.7	13.7	7.35
Si	20.2	33.1	13.1	7.04	10.1

*(Hamaker constants were not available as force data for PA66 - PA66 and PA12 – PA12 interactions could not be obtained reliably.)

While radii of contact calculated separately for each tip-surface pair yielded unreasonably small values, we investigate whether trends in forces versus calculated work of adhesion can yield better estimates. Contact mechanics theories (JKR or DMT) predict that plotting the measured adhesion forces F against the work of adhesion $\Delta\gamma$ for a series of materials should yield a line with slope proportional to R if the elastic moduli (and hence chemical structure are similar for these materials.

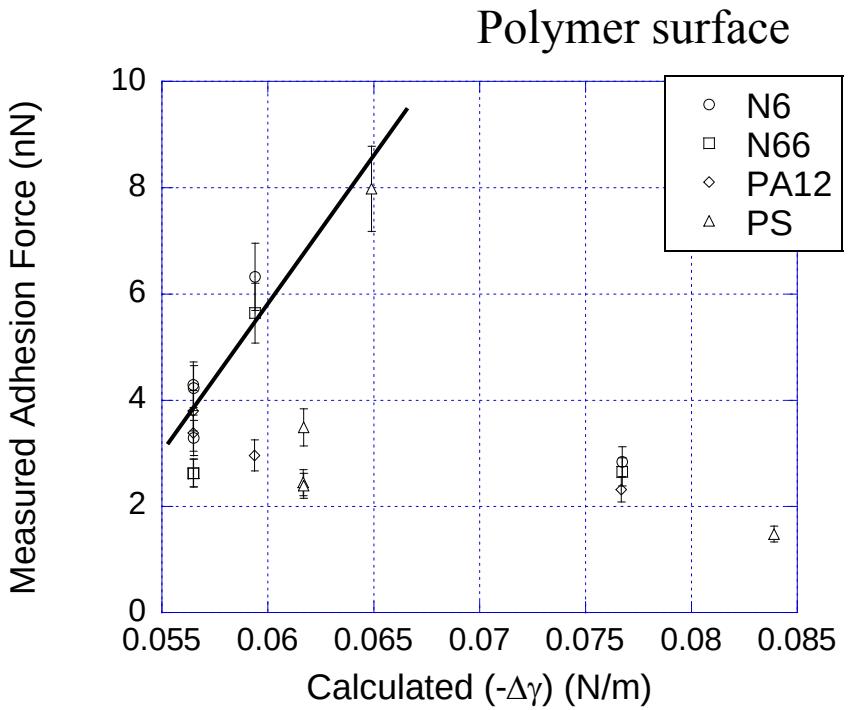

Figure 3 – 5. Measured pull-off forces correlated against calculated work of adhesion for interactions between modified and unmodified AFM probes on various polymeric surfaces (PA6, PA66, PA12 and PS).

We plotted the measured F values versus the Lifshitz-calculated $\Delta\gamma$ in Figure 3-5. The results indicate that for this polymer series F does not in general scale linearly with

the respective $\Delta\gamma$. However, a subset of the tip-coating / surface combinations (PS/PS, PS/PA6, PS/PA66, PA6/PA6, PA6/PA12, PA66/PA12, PA6/PA66 and PA12/PA66) yield a line with slope of 250 nm. For those pairs of tip coatings and surfaces whose adhesion force values scale linearly with $\Delta\gamma$, dividing the slope value by 1.5π or 2π (JKR or DMT) yields a contact radius of 50 nm or 40 nm, respectively. Feldman[46] observed a similar scaling for a series of polymers (PS, i-PP, PVDF and FEP) interacting with a SiO_x AFM tip. They calculated a contact radius of 51 nm assuming a JKR model, in close agreement with our value using the same model. These values are also lower than the $R_{Approach}$ obtained from the approach curves, but are 2 to 5 times larger than the radii calculated directly from the JKR, DMT, and PT-FDR models for each of the tip-surface pairs. The polymers that fall on this line include all of the self-interactions, all of the polyamide-polyamide interactions, and interactions between with PS-tip and PA-surface (with the exception of the softest and most hydrophobic, PA12). This is expected since JKR and DMT theory were derived strictly to model the relationship of F vs. R for constant $\Delta\gamma$, e.g., when the tip and surface coatings are the same. The other group of tip coatings and surfaces (PS/PA12, PA6/PS, PA66/PS, PA12/PS, Si_3N_4/PA6, Si_3N_4/PA66, Si_3N_4/PA12 and Si_3N_4/PS) show no significant relationship between F and $\Delta\gamma$. We note that this series shows the largest differences in tip versus surface chemical nature and moduli.

3.3 CONCLUSIONS

We applied atomic force microscopy to measure adhesion forces between polyamides and various surfaces by coating AFM tips with the respective polymers. We observed a discrepancy in "mirror-image" force measurements between coated AFM tips and flat coatings. Namely, chemically dissimilar polymers show significantly different interaction forces depending on the placement of each polymer on the tip versus on the flat surface. The strongest differences were shown between PS and PA, in which the force for PS(tip)- PA(surface) was three-times larger than the reversed PS(surface)-PA(tip) situation. This phenomenon could be a significant effect in AFM-based measurements of interactions between dissimilar materials. Developing methods or models to circumvent this difficulty is an important subject for future research. We found that a simple Hamaker-type model of a square pyramidal tip interacting with a flat substrate (SPFS) gave radii of contact that were in the range expected for AFM measurements and lead to Hamaker constants in the appropriate range for this class of materials. Three other adhesion models (the JKR, DMT and PT/FDR) gave smaller contact radii estimates that subsequently would lead to overestimated Hamaker values. JKR and DMT theory yield a contact radius close to that of the SPFS when *trends* in the relationship of force and work of adhesion are plotted for a series of similar chemistry, instead of making calculations for each data point. In this case the slope of F vs $\Delta\gamma$ is equal to $1.5R$ (JKR) or $2R$ (DMT).

CHAPTER IV

QUANTIFICATION OF *E. coli* ADHESION TO POLYAMIDES AND POLYSTYRENE WITH ATOMIC FORCE MICROSCOPY

Atomic force microscopy (AFM) was used to measure adhesion forces between *E. coli* bacteria and surfaces consisting of a series of polyamides and polystyrene, materials that are prominent in carpeting, upholstery and other indoor surfaces. Bioparticle adhesion to such surfaces in air is poorly understood, yet these interactions are thought to play a key role in their accumulation and release as indoor air pollutants. The polymers employed were polyamide 6 (PA6), polyamide 6,6 (PA66), polyamide 12 (PA12) and polystyrene (PS). We report the interaction forces between immobilized *E. coli* and AFM tips coated with each polymer. The adhesion forces for the tip-bacterial interactions were in the range between 2.9 and 6.7 nN, which is of the same magnitude as the polymer-polymer interactions for the same series of polymers. Polystyrene had stronger adhesion with *E. coli* than any of the three polyamides, by an average factor of 1.4. The work of adhesion and Hamaker constants of the probe – surface interactions were calculated using a square-pyramid flat-surface model developed previously. With these values, we determined the average *E. coli*-polyamide adhesion ($F \sim 4nN$) is about the same strength as polyamide-polyamide adhesion. Ordinary indoor activities such as foot traffic are estimated to be unlikely to generate enough draft ($F \sim 0.2\ nN$) to release the cells into the air from the polymer surfaces. However, higher air flow rates induced

by many commercially available vacuum cleaners appear to be sufficient to remove particles from the surfaces ($F \geq 30\ nN$).

4.1 INTRODUCTION

Atomic force microscopy (AFM) has been adapted in recent years to measure interactions between particles and surfaces. Ducker et al[88] first reported in 1991 the use of a 'colloid probe' technique where the AFM tip was replaced by a particle of known geometry and composition as a means to measure directly the force between a planar surface and an individual colloid particle. Other researchers applied this method to investigate the discrepancies between theoretical DLVO force curves and AFM pull-off forces in electrolytes.[89] This technique was later extended to immobilize a single microbial cell at the apex of a tipless cantilever to produce cell probes for bio-adhesion studies.[90] Reviews[79, 91] indicate that the majority of studies report cell-surface interactions in aqueous environments. For relevance to air quality, we are interested in bioparticle – surface interactions in air.

In the previous chapter, we reported a methodology for coating AFM tips with polymers and then using these coated tips for measurements of polymer-polymer adhesion forces.[92] This approach is extended here to measure the adhesive interactions of *E. coli* with AFM tips coated with Nylon-6 and Nylon-6,6, materials prevalent in indoor environments as carpeting and upholstery. In addition to bare AFM tips, polystyrene- and polyamide-12-coated tips were used as controls for comparison. We also present

calculations for the effective contact radii and Hamaker constants of the bacterial – polymer interactions in air.

4.2 EXPERIMENTAL MATERIALS AND METHODS

4.2.1 POLYMER FILM SAMPLES AND PREPARATION

A series of thin polymer films were prepared on piranha-etched silicon to be used as substrate for this study. These consisted of polystyrene, (PS, average molecular mass = 100,000, Avocado Research Chemicals, Lancashire, England), Nylon 6, (PA6, average molecular mass = 10,000, Aldrich Chemical Co., Inc., Milwaukee, WI) and Nylon 6/6 (PA66, average molecular mass = 22,000, Aldrich Chemical Co., Inc., Milwaukee, WI). Polyamide 12 (PA12, average molecular mass = 40,000, Atofina Chemicals, Philadelphia, PA) is included in this study to investigate the effect of amide structure on interactions. The PS solution was prepared by dissolving 10% by mass in toluene while 1% by mass PA6, PA66 and PA12 solutions were prepared in hexafluoroisopropanol (HFIP, TCI America, Portland, OR). Polymer films were made by a knife-edge coating technique described in detail elsewhere [66, 67]. Films were annealed at 80 °C under vacuum for 2 hours.

4.2.2 AFM PROBES AND THEIR MODIFICATIONS

The AFM used was a Thermomicroscopes™ Explorer (Veeco Metrology Inc., Santa Barbara, CA). Standard V-shaped silicon nitride cantilevers from Veeco of spring constant 0.10 N/m were used for the force spectroscopy. The scanner has a Z range of 10 μm. A micromanipulator was used in conjunction with a binocular microscope (magnification 20x) to dip AFM tips into a dilute polymer solution (~1 wt %) resulting in a coated tip, as described previously.[92] The coated tips were dried in air for one day before being used for the force measurements. The same tip was used to measure all bacterial – tip interactions within a given polymer series, to ensure a constant spring coefficient. Prior to the force measurements, the AFM was used in imaging contact mode to determine that the *E. coli* on the polymer surface were non-overlapping. Force measurements were taken on the top of randomly selected intact cells. SEM images of the modified AFM tips were shown previously[92] and we demonstrated that the polymer layers on the tips were sufficiently thick to screen out the effect of the silicon nitride.

4.2.3 BACTERIAL STRAIN, GROWTH CONDITIONS, AND HARVESTING

The gram-negative strain *E. coli* DH5αpro, which occurs commonly in the human body, was obtained from Andreas Bommarius' lab at Georgia Tech. *E. coli* was grown aerobically in agar broth nutrient (EMD Biosciences, San Diego, USA) at 37^{o}C. The bacteria were harvested by centrifugation (5 min at 10,000 x g), washed twice with deionized water, and resuspended in water. A droplet of bacterial suspension (5 – 10 μL) was placed onto the chosen substrate and left to dry in ambient air for about a day. The concentration of the bacterial suspension was ~ 10^8 – 10^9 mL^{-1}.

4.2.4 CONTROL OF HUMIDITY

For the AFM force measurements in air, humidity and grounding of the sample surface are important in order to control static electrical charges. The AFM was enclosed in a humidity-controlled acrylic chamber. The relative humidity (RH) in the laboratory has a typical relative humidity of 20 – 35%. This variation was unacceptable and led to cases of unwanted electrostatic potential forces. For our measurements at room temperature the RH within the chamber was held at 40%. Higher humidity might cause capillary effects to become significant but these tend to occur when the relative humidity is above 65% [68].

4.2.5 FORCE MEASUREMENTS

In the previous chapter we reported force measurements made between both coated and unmodified AFM tips and control surfaces composed of the polymers under study here.[92] That study indicated the reliability of the coated-tip AFM measurements and enabled the development of a model for calculation of contact radii and Hamaker constants with coated AFM tips. In this chapter, the interactions between the same coated AFM tips used previously and immobilized *E. coli* were measured in air. To investigate potential effects of the substrate, we considered *E. coli* immobilized on four different surfaces (PA6, PA66, PS and Si). For a set of specific tip-surface force measurements, 30 force curves were taken randomly from intact *E. coli* cells on two

separate wafer surfaces within three 10 μm by 10 μm areas on each surface. From the force versus distance measurements, a calculation based on the Square Pyramid Flat Surface model (SPFS) developed in our previous publication[92] was performed to estimate Hamaker constants, contact radii and work of adhesion for the different tip – bacterial surface interactions.

4.2.6 SCANNING ELECTRON MICROSCOPY (SEM)

SEM (Hitachi Model S-800) was used to confirm that the modified tips were indeed coated with the respective polymers. The tips were mounted on to metal stubs using carbon tape before imaging using an accelerating voltage of 10 kV.

4.3 RESULTS AND DISCUSSIONS

Table 4 – 1 shows the average forces obtained for each tip and *E. coli* / substrate combination studied. For comparison, these raw forces are of similar magnitude and range as the forces that we measured for the corresponding polymer-polymer interactions (1.5 to 8 nN using the same coated tips), published previously.[92]

Table 4 – 1. Adhesion Force distributions (at 95% confidence interval) for various tip–bacteria-surface interactions.

	Adhesion Force (nN)				
	AFM Tip Coating				
Bacterial Surface	Si_3N_4	PA6	PA66	PA12	PS
PA6	3.7 ± 0.4	4.9 ± 0.8	3.1 ± 0.3	3.6 ± 0.3	5.2 ± 0.6
PA66	3.9 ± 0.5	3.5 ± 0.5	*	3.4 ± 0.4	5.3 ± 0.6
PA12	4.0 ± 0.5	*	*	4.2 ± 0.4	6.7 ± 0.5
PS	3.4 ± 0.5	3.5 ± 0.4	2.9 ± 0.3	2.9 ± 0.2	4.7 ± 0.6
Si	4.1 ± 0.5	5.2 ± 0.6	4.8 ± 0.5	4.1 ± 0.5	5.5 ± 0.7

*Force data for the PA66 - PA66, PA6 – PA12 and PA66 – PA12 interactions could not be obtained reliably.

The Si_3N_4 unmodified tip data (1st column on left of Table 4 – 1) indicates that changes in the substrate under the *E. coli* did not change the bacteria-probe interaction. However, for the other tip coatings, the measured force was different depending on the substrate the bacteria were deposited onto. The *E. coli* deposited on polystyrene had the weakest adhesion forces for the same set of coated tips, compared to *E. coli* on other polymeric surfaces, while bacterial cells on silicon wafers exhibited the strongest adhesion to the AFM tips with the exception of cells on the PA12 surface. These observations suggest that the underlying substrate may affect the presentation of chemical groups or the physical morphology of the *E. coli* surface. For this reason, comparisons between various tip-coatings should only be made within the set for the same supporting substrate.

Regardless of the underlying substrate, however, a number of trends are apparent. In the majority of cases, the polyamide (PA6, PA66 and PA12) adhesion forces were comparable to or less than those of the unmodified silicon nitride tip. The force distributions of the three types of polyamides-coated tips do not differ significantly from each other, although PA6 displayed the strongest adhesion force among them. The polystyrene (PS) tip showed the strongest adhesion to the bacteria – stronger than the polyamide-coated and unmodified tips. This might appear surprising given the presence of hydrogen-bonding and polar groups in the polyamide. *E. coli* have an approximate cell surface composition of ¾ sugar oligomers and ¼ proteins.[93] The amphiphilic character of the oligosaccharides means that different kinds of forces may be involved in their interactions with various surfaces. The presence of hydroxyl groups on the sugars would allow intermolecular hydrogen bonding with the polar amide bonds of the Nylons. Single molecule sugar ligand-protein interactions are typically a mix of hydrogen bonds (< 7 kcal/mol[94]) and van der Waals contacts,[95] and require multi-valency and water[96] to maintain strong bonding and stability.[97, 98] Alternatively, it is well-known that non-polar C-H bonds can engage in weak charge-transfer complexes with π orbitals such as those in phenyl rings[99]. This CH/ π interaction, while weak (~ 1 kcal/mol) for single molecules, becomes significant for macromolecules with multiple interacting groups. Most importantly, unlike hydrogen bonds, CH/ π interactions can take place in both polar and non-polar media. In addition, the CH/ π interactions benefit entropically from the many symmetrical configurations possible between CH and flat π-orbital systems, whereas hydrogen bonds require a much smaller range of molecular orientations. Fernández-

Alonso and co-workers provided an in-depth study of the physicochemical nature of sugar-aromatic interactions and showed that the C-H/π complex is stable from both theoretical and experimental viewpoints.[55] These observations suggest at least one plausible reason for the observed strong interaction between the bacterium surface and the PS aromatic rings.

In addition to specific interactions, it is likely that PS simply has larger VDW dispersion interactions with *E. coli* than the polyamides. From our earlier work[92] comparing PS and polyamide self- and cross-interactions, the measured Hamaker constants were always higher if one of the surfaces was PS. For example, PA6-PS had a higher Hamaker constant (and adhesive force) than PA6-PA6 or PA66-PA66.

To see if surface roughness of the bacterial surface plays a role in the adhesion force, roughness was measured using the AFM and the results are displayed in Table 4-2. The average roughness (Ra) values for the bacteria surfaces ranged from 11 to 14 nm and were statistically indistinguishable from one another. The results indicate that the polymer substrate the cells reside on does not influence the roughness or topography of the *E. coli*. This suggests that *E. coli* surface chemistry rather than surface roughness would play the dominant role in the tip-cell surface interactions.

Table 4 – 2. Surface roughness of the bacterial surfaces deposited on different polymers calculated using the AFM with 95% confidence intervals.

Surface	N 6	N 66	PA 12	PS	Si
Ra (nm)	14.4 ± 1.3	10.9 ± 1.0	11.1 ± 1.0	12.5 ± 1.1	12.2 ± 1.1
RMS (nm)	18.3 ± 1.5	13.7 ± 1.1	15.1 ± 1.2	16.0 ± 1.3	15.2 ± 1.1

In addition to lipopolysaccharides which cover about 75% of the bacterium's surface, many bacterial cells also have proteins on their outer membrane. Each individual AFM measurement would be taken at a different contact area and thus the chemical bond interactions with the AFM tip could be different even if the measurements are made on the same bacterium. Thus variations in adhesion force and pull-off distances should occur at the single cell level, in a population of cells on a polymer substrate surface, and on cells in different polymer substrate surfaces. We did not isolate the three scenarios to compare their variations, but the scatter in our data was consistently seen to be a 95% confidence interval of +/- 10% of average values.

We also considered the cell shape and curvature, whether the cells had been lysed accidentally, or if the cell wall had collapsed during the harvesting, centrifuging and drying processes. Figure 4-1 shows two AFM contact mode images of the bacterial cells on a polystyrene substrate. Some bacterial cells (Fig. 4-1b) had lysed during sample preparation. Thus prior to AFM force measurements, a contact mode scan was used to

determine that the AFM tip would be approaching at the flattest part of intact bacterium surfaces.

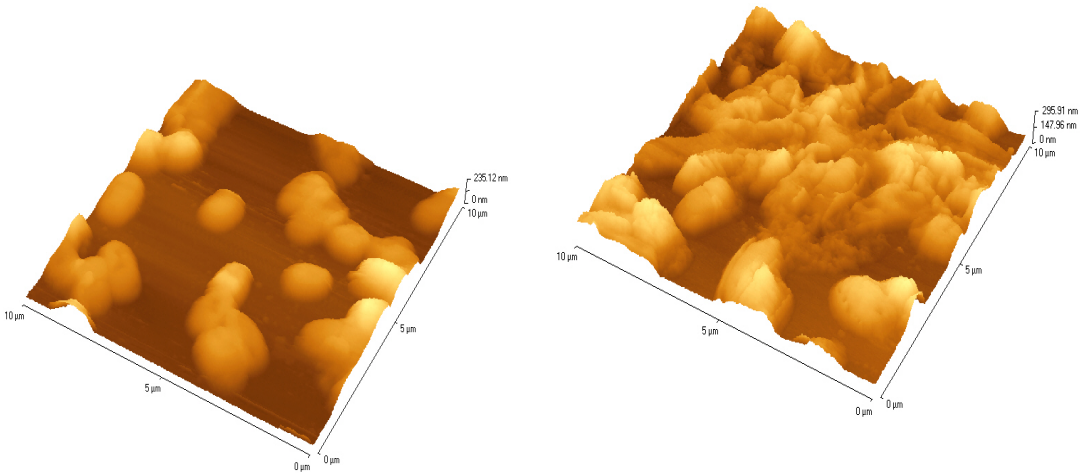

Figure 4 – 1. Typical AFM contact mode images of *E. coli* deposited on a polystyrene polymer substrate surface: (a) 10 µm x 10 µm scan area with 0 to 235 nm height (linear from darkest to lightest) and (b) 10 µm x 10 µm scan area with 0 to 296 nm height (linear from darkest to lightest).

The pull-off distances for the different polymer coated AFM tips varied between 400nm to about 800nm. The PS-coated tip had the longest pull-off distance, which is consistent with the adhesion force distribution. For the other tip-cell surface combinations, there are no obvious trends between polymer and pull-off distances (Figure 4 – 2).

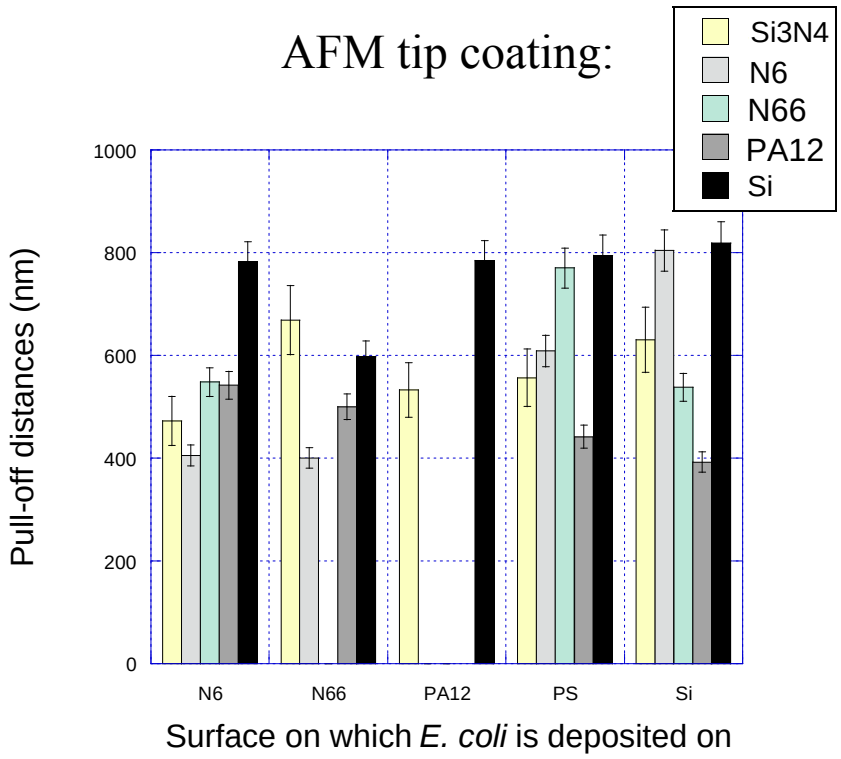

Figure 4 – 2. Pull-off distance distributions for tip-bacteria surface interactions presented in Table 4 – 1.

4.3.1 MODELING OF ADHESION FORCE DATA

We applied the SPFS model to the adhesion force data to calculate the radii of contact and Hamaker constants between *E. coli* and the coated AFM probes, shown in Table 4 – 3.

Table 4 – 3. Calculated parameters for the SPSF model for interactions between *E. coli* immobilized on various polymer surfaces and modified AFM probes. Uncertainties are 95% confidence intervals.

AFM tip	Surface	$R_{contact}$ (nm) (SPFS)	$A_{tip\text{-}bact}$ ($J \times 10^{20}$)	$A_{polymer\text{-}polymer}$ ($J \times 10^{20}$)
Si_3N_4	PA6	17.2 ± 1.7	16.1 ± 3.5	13.3
Si_3N_4	PA66	17.2 ± 1.0	24.6 ± 7.7	13.3
Si_3N_4	PA12	14.6 ± 1.2	25.4 ± 6.3	13.3
Si_3N_4	PS	9.6 ± 0.6	55.0 ± 15.3	14.6
Si_3N_4	Si	18.8 ± 1.7	19.3 ± 2.7	41.5
PA6	PA6	27.6 ± 2.1	7.1 ± 2.3	7.9
PA6	PA66	22.5 ± 2.7	8.3 ± 2.2	7.9
PA6	PS	37.5 ± 1.6	3.7 ± 0.5	8.6
PA6	Si	31.8 ± 2.0	10.6 ± 1.8	23.4
PA66	PA6	34.1 ± 2.3	3.8 ± 0.9	7.9
PA66	PS	29.5 ± 2.5	7.0 ± 1.3	8.6
PA66	Si	19.8 ± 1.5	18.5 ± 6.2	23.4
PA12	PA6	39.2 ± 3.3	3.4 ± 0.8	7.9
PA12	PA66	30.4 ± 2.9	5.4 ± 1.6	7.9
PA12	PS	33.4 ± 2.9	3.2 ± 1.0	8.6
PA12	Si	14.6 ± 1.0	19.4 ± 3.8	23.4
PS	PA6	30.2 ± 2.5	12.8 ± 3.4	8.6
PS	PA66	25.4 ± 3.1	14.1 ± 3.4	8.6
PS	PA12	24.2 ± 2.5	26.7 ± 9.2	8.6

Table 4 – 3 (continued)

AFM tip	Surface	$R_{contact}$ (nm) (SPFS)	$A_{tip\text{-}bact}$ (J x 10^{20})	$A_{polymer\text{-}polymer}$ (J x 10^{20})
PS	PS	34.8 ± 1.0	7.7 ± 1.3	9.4
PS	Si	16.8 ± 0.5	40.9 ± 7.3	25.7

Contact radii ranged between 10 nm to 20 nm for the bare tip and between 20 nm to 40 nm for the polymer coated tips. This observation is reasonable, since the polymer coating is expected to reduce the curvature slightly by covering the sharp Si_3N_4 tip. The polymer-bacterial Hamaker values ($A_{tip\text{-}bacteria}$) ranged between 3 to 55 x10^{-20} J, with the highest values observed for bare Si_3N_4 tips. Other studies that have computed Hamaker constants using AFM force data for biological[100] and non-biological systems[46] were performed in liquid (aqueous) media. Hence, as expected, those values are about a magnitude smaller than the $A_{tip\text{-}bacteria}$ we report here for interactions in air. In general Hamaker constants between two similar surfaces in air are larger than those in liquid medium, and the usual result for water versus air is about 1 order of magnitude smaller in water. Table 4-3 also shows, for comparison, the Hamaker constants we measured previously for the same polymer-coated tips and neat polymer surfaces in air.[92] These indicate that polymer-*E. coli* interactions in air are about the same magnitude as the corresponding polymer-polymer interactions, providing a type of 'calibration' for the forces encountered.

While a fully detailed model of the effect of these adhesion forces on particle distributions in air is beyond the scope of this work, it is possible to use the

measurements to provide meaningful boundary conditions. For example, Hamaker constants can be used to estimate the energy of adhesion per unit area between 2 flat surfaces, $\Delta\gamma$, by the relation:

$$\Delta\gamma = \frac{A_H}{12\pi D_0^2} \qquad (4-1)$$

where D_0 = 0.165 nm is the nominal value used for cutoff separation.[42] Applying this relation to the case of an *E. coli* – PA6 interaction which has a $A_{tip\text{-}bact}$ value of about 7 x 10^{-20} J as shown in Table 3. From equation (4 – 1), $\Delta\gamma$ is 0.068 J/m^2. As already pointed out for the raw force data (Table 4 – 1), this work of adhesion is very similar to the range of values measured in our previous study of polymer-polymer interactions.[92] Hence, bacterial-polyamide adhesion is about the same strength as polyamide-polyamide adhesion.

One significant question related to indoor air quality is whether adhesive energies of this magnitude will prevent the redistribution of bacteria adhered to surfaces into the air under normal air flows. One approach is to estimate typical air flow velocities and use this to calculate the drag force on a model particle, then compare that drag force to the measured adhesive forces to see which is greater. Presumably, if the air-flow-induced drag force is significantly higher than the adhesive force, the particle may be lifted free of the surface. The average measured adhesion force between a cell and the PA6-coated tip is about 4 nN from Table 4 – 1. This adhesion force is about 10^6 times greater than the bacterium's weight (~3 x 10^{-15} N).

The drag force on a smooth sphere is given by[101, 102]:

$$F_D = C_D A_P \rho \frac{v^2}{2} \qquad (4-2)$$

where ρ is the fluid density (ρ_{air} = 1.2 kg/m³ at sea level), v^2 is the air velocity, A_P is the projected surface area, and C_D is the drag coefficient (a function of the Reynold's number). We estimate the air velocity created by compression of a nominal 1 cm thick carpet pile by a foot step in the following manner. Using a nominal foot size of 10 cm by 30 cm, multiply by the pile thickness (1 cm) and assuming it is compressed in 0.1 s, leads to a volume flow rate of 0.003 m^3/s. If this volume of air is released from the sides of the compressed carpet, then the resulting velocity is v = 0.32 m/s (independent of carpet height). Assuming that the bacterium is a sphere with a diameter of D = 1 μm, and taking the air viscosity to be $\mu = 1.8 \times 10^{-5}$ Pa s, the Reynold's number is $Re = Dv\rho/\mu$ = 0.025. Since this is well within the regime of Stoke's flow, $C_D = 24/Re$ = 960, resulting in a drag force F_D of 0.25 nN. This drag force is smaller than the forces measured here for bacteria-polymer adhesion, ~ 4 nN, indicating that air flow induced by foot traffic is probably insufficient to release adhered *E. coli* from Nylon (polyamide) carpeting. For comparison, consider that many commercially-available vacuum cleaners specify air flow rates (in the hose) in excess of 100 miles per hour, or v = 44 m/s. This velocity yields a drag force of 37 nN, which is sufficient for removing particles that adhere with a 4 nN attractive force.

4.4 CONCLUSIONS

We have reported measurement of adhesion forces between *E. coli* and polymers used in synthetic carpeting, upholstery, and other indoor surfaces. Using a simple Hamaker-type model of a square pyramidal tip interacting with a flat substrate (SPFS) developed previously, we estimated the work of adhesion and Hamaker constants of the probe-surface interactions. These values were the same magnitude as the polyamide self interactions. Among the polymers we employed polystyrene-coated tips showed the strongest adhesion with the bacterial surfaces, averaging about 1.4 times stronger than polyamide-coated tips. One of the plausible reasons is the presence of the carbohydrate-aromatic interactions between the bacterium cell surface and PS aromatic rings. Additionally, PS has larger VDW dispersion forces compared to the polyamides.[92]

The significance of the measured forces to indoor air quality can be estimated by comparing to drag forces encountered in normal household activities. The magnitude of the bacteria-polymer adhesion forces probably prevents their detachment due to air flow induced by foot traffic. However, higher velocities induced by cleaning (vacuuming) appear to be sufficient to remove particles. Knowledge gained from such investigations will not only assist our understanding of bioparticle – polymer interactions, but may also lead to useful strategies for the design of indoor carpet polymer material properties for the improvement of indoor air quality by trapping undesirable bio-particulates.

CHAPTER V

CHARACTERIZATION OF RAGWEED POLLEN ADHESION TO POLYAMIDES AND POLYSTYRENE USING ATOMIC FORCE MICROSCOPY

The adhesive behavior of short ragweed (*A. artemisiifolia*) pollen grains to polymers was studied by means of atomic force microscopy (AFM). The polyamides were chosen due to their use in synthetic carpet, while pollen allergens are a leading cause of asthma and allergies in the indoor environment. Polymers employed in our study were Nylon 6 (N6), Nylon 6,6 (N66) and polyamide 12 (PA12), with polystyrene (PS) and silicon as controls. Single pollen grains were attached to the tip of an AFM cantilever, which was then used to measure the pollen adhesion force with polymers of interest. Humidity and pollen compliance were investigated as potential artifacts, but were shown to be insignificant under the measurement conditions. A typical pollen grain had an average adhesion force of 10 ± 3 nN to a flat polymer surface, independent of surface type. We conclude that van der Waals forces are the primary mechanism for adhesion and that the number of contacts formed, and hence the total force, is controlled by the presence of spiky growths on the pollen surface.

5.1 INTRODUCTION

Indoor air quality is an important factor in respiratory health, especially asthma, which affects 20 million people at a cost exceeding $10 billion annually in the US alone.[103, 104] Floor coverings and upholstery are thought to have a dramatic effect on the indoor accumulation and distribution of biological allergenic particulates (mold, dust

mites, pet dander, and pollen). Airflow models have suggested that carpeting has a positive effect on air quality because particles adhere to fibers and this is thought to hinder their release back into the air. However there is also disagreement about this conclusion[6], which may reflect several significant unknowns: differences in adhesion due to particle origin (species), shape (fragments versus whole particles), carpet material (N6, N66 or PET), and the presence of soil- and stain-resistant treatments. Perhaps the most significant unknowns are the adhesive force magnitude and mechanism.

Pollens represent the most important source of natural allergens[105], yet very little is known about their adhesion to carpet, let alone to synthetic polymer material. Proteins from flowering-plant pollen grains are well-known allergens with their adverse human health effects.[106, 107] Significant allergenic pollens include ragweed (*Ambrosia*), grasses (*Poacea, Phleum*), and birch (*Betula*). All are from wind-pollinating plants, and the massive production and dispersion of pollen grains into the atmosphere is a main contributor to allergies.[108] While exposure to such natural allergens is unavoidable, it is desirable to design protective and preventative measures to minimize their negative impact. Understanding the adhesion of pollen grains to polymer surfaces is an important aspect in designing modified indoor surfaces.

Since the invention of atomic and lateral force microscopy (AFM and LFM) in the 1980s[109], researchers have used both techniques extensively to characterize nanometer-scale, surface chemical interactions in the field of microbiology[35, 79]. AFM provides quantitative, real-time, spatially-resolved information on the interactions

between the scanning probe and the sample surface at ambient conditions. In this study, the 'colloidal' AFM probe method developed by Ducker *et al*[88] has been adopted to measure the adhesion forces of ragweed pollen with polymers widely used in carpet: Nylon 6 and Nylon 6,6. Force measurements of the pollen grains interacting with the polymer surfaces were used to understand the general behavior of pollen adhesion to surfaces. Polystyrene, polyamide-12 and silicon were included as controls for comparison.

5.2 EXPERIMENTAL SECTION: MATERIALS AND METHODS

5.2.1 POLYMER FILM SAMPLES AND PREPARATION

Thin polymer films were prepared on Piranha-etched silicon wafers. These included polystyrene, (PS, average molecular mass = 100,000, Avocado Research Chemicals, Lancashire, England, average molecular mass = 2330, 3680 and 114200, Aldrich Chemical Co., Inc., Milwaukee, WI), Nylon 6 (PA6, average molecular mass = 10,000, Aldrich Chemical Co., Inc., Milwaukee, WI), Nylon 66 (PA66, average molecular mass = 22,000, Aldrich Chemical Co., Inc., Milwaukee, WI), and polyamide 12 (PA12, average molecular mass = 40,000, Arkema Group, Philadelphia, PA). The PS solution was prepared by dissolving 10% by mass in toluene while 1% by mass PA6, PA66 and PA12 solutions were prepared in hexafluoroisopropanol (HFIP, TCI America, Portland, OR). Polymer films were made by spin casting the solutions onto the silicon wafers at 1000 rpm for 30s, followed by annealing in a vacuum oven at 100 ^{o}C for 2 h.

Measurements of film thickness are not reported here, but they exceed the range of van der Waals interactions (10 nm) to negate any effects by the underlying silicon substrate on the polymer-pollen interactions.

5.2.2 CONTACT ANGLE MEASUREMENT

Static contact angles for water were measured on the different polymer films using a video contact angle 2500XE system (AST products, Billerica, MA). A 1 μl drop was dispensed separately onto the sample surface. Both the right and left angles between the sample surface and the tangent line to the droplet were measured.

5.2.3 POLLEN

Short ragweed (*A. artemisiifolia*) non-defatted pollen grains were purchased from Greer Labs (Lenoir, NC) and stored at 4 ^{o}C prior to use. Some dry pollen grains were frozen in Tissue-Tek® O.C.T. (Optimal Cutting Temperature) Compound (Tissue-Tek, 4583, Sakura Finetek, Torrance, CA, USA), and cut into 5-µm thick sections using a cryostat (Cryo-Star HM 560 MV, Microm, Waldorf, Germany) for examination of their cross-sections using the scanning electron microscope.

5.2.4 ATTACHMENT OF POLLEN GRAINS TO AFM PROBES

Three sets of AFM measurements with the polymer surfaces were conducted on a Pico Plus atomic force microscope (Molecular Imaging Inc., Tempe, AZ). Tipless rectangular cantilevers with nominal spring constants of 0.02 – 5 N/m (Applied NanoStructures, Inc., Santa Clara, CA) were used. Single pollen grains were glued to the AFM cantilevers with a small amount of epoxy resin using a procedure described in detail elsewhere.[88] The cantilevers with pollen-grain attached are shown in Figure 5 – 1. Three tipless cantilevers each with a pollen grain attached to the free end were used for the adhesion force measurements. The actual spring constants for the cantilevers with the attached pollen grains were determined separately to be 0.007, 0.009 and 0.576 N/m using the thermal spectrum fit methods of Burnham[110] and Hutter et al[111]. About 25 force-distance curves were measured for each pollen tip and polymer surface combination, taken on three separate polymer samples within three randomly chosen 10 μm by 10 μm areas on each polymer substrate surface.

Two additional pollen-attached cantilevers (pollen grains 4 and 5) with spring constants of 0.29 and 0.65 N/m respectively were used for compressive tests on Si under varying humidity with a Nanoscope IIIa (Veeco, Santa Barbara, CA) scanning probe microscope. The details are given in the next two sections.

5.2.5 CONTROL AND VARIATION OF RELATIVE HUMIDITY

Unless specified otherwise, relative humidity in the laboratory under ambient conditions for the Pico Plus AFM force measurements was at 40%. The Nanoscope IIIa

AFM was enclosed in a humidity-controlled glass chamber. To see the impact of humidity on the AFM force measurements, the relative humidity was varied for two sets of controlled adhesion force experiments involving pollen grains 4 and 5 on hydrophilic piranha-etched silicon wafers. Relative humidity of 20% and 60% was achieved separately by flowing pure nitrogen gas to the positive pressure chamber of Nanoscope IIIa in the former and bubbling the nitrogen gas through two glass columns of water for the latter.

5.2.6 COMPLIANCE TESTING OF THE POLLEN GRAINS

All 5 pollen grain-attached AFM cantilevers were subjected to varying applied force loadings to determine the point of their compliant yielding. This was done to ensure that force measurements were taken only in the region where the pollen grains were not deformed by the applied force. The typical applied load for our force measurements during contact was 2.4 ± 0.3 nN, and no permanent deformation of the pollen grain tip-cantilevers were found (Figure 1). Figure 5 – 2 shows the maximum applied loads and retraction curves of pollen grains 4 and 5 on a silicon surface at 20% and 60% relative humidity, and no compliance of the grains was observed for the approach curves. The plateaus in Figures 5 – 2(a), (b) and (d) indicate that the limit for the photo detector was reached and that the average maximum pressure was around 0.5 GPa if we assume only one spike was in contact with the surface.

5.2.7 SURFACE ROUGHNESS

To investigate whether surface roughness was a factor in the adhesion force measurements, we used a Thermomicroscopes™ Explorer AFM (Veeco Metrology Inc., Santa Babara, CA) with V-shaped silicon nitride cantilevers of nominal spring constant 0.10 N/m to measure the mean (Ra) and root-mean-square (RMS) roughness of each surface-coating. For each of three random 10 μm x 10 μm scans of the substrate surfaces, the image was split into 4 sectors for a total of 12 roughness measurements.

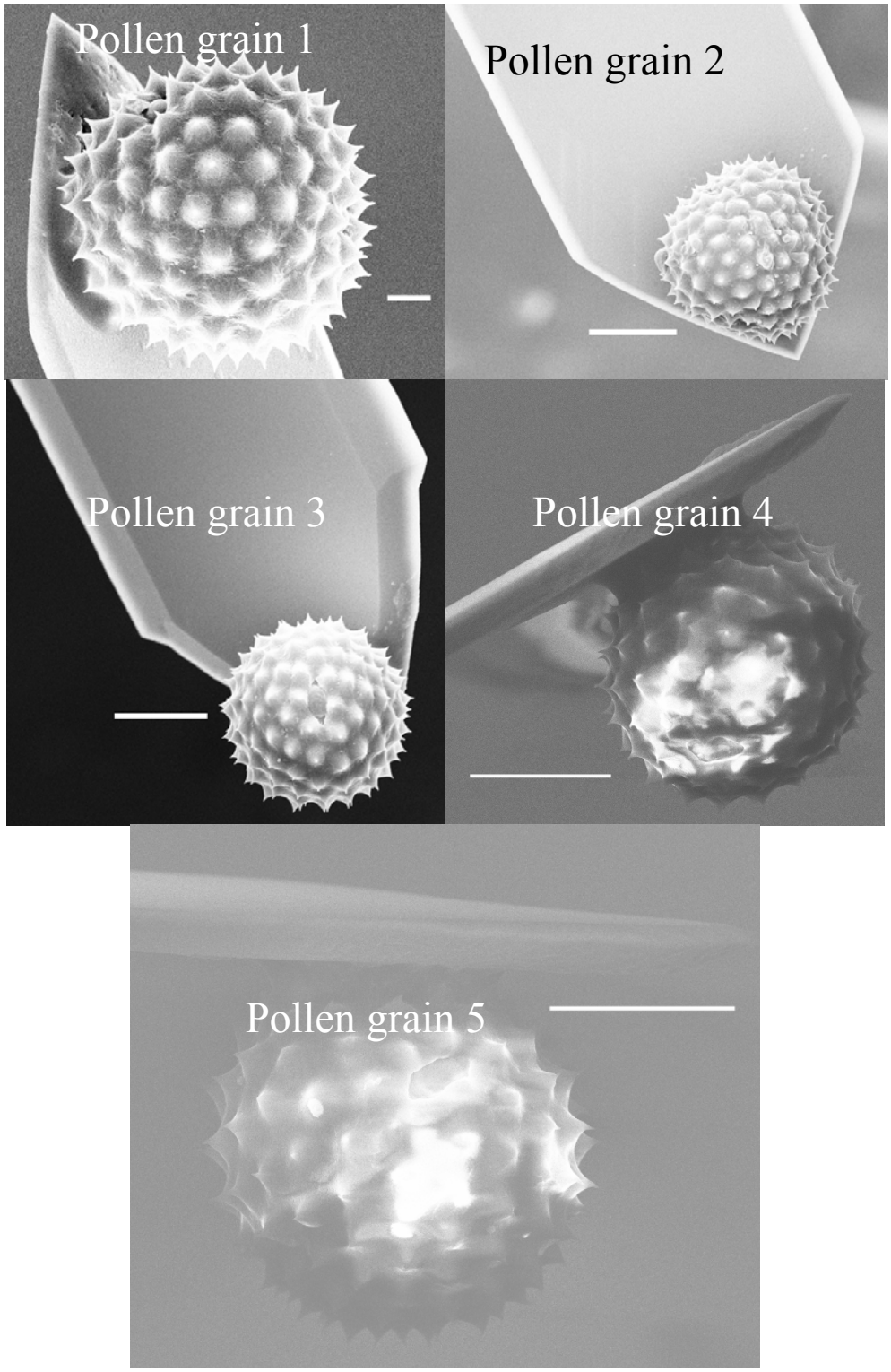

Figure 5 – 1. Scanning electron micrographs of ragweed pollen grains glued to the end of tipless AFM cantilevers. The white scale bar represents 3 μm for pollen grain 1 and 10 μm for grains 2 – 5. Pollen grains 4 and 5 were not sputtered with gold prior to the SEM imaging. Note the absence of any visible contamination on all 5 cantilevers' pollen surfaces after repeated force measurements with multiple surfaces.

5.2.8 SCANNING ELECTRON MICROSCOPY (SEM)

The modified 'colloidal' AFM probes were characterized by scanning electron microscopy (SEM) (LEO 1530 FEG). This was done after *all* force measurements were finished on PA6, PA66, PA12 and PS. Only pollen grains 1 – 3 were sputtered with gold; all 5 probes were mounted on metal stubs using carbon tape and an accelerating voltage of 10.0 kV was applied before imaging.

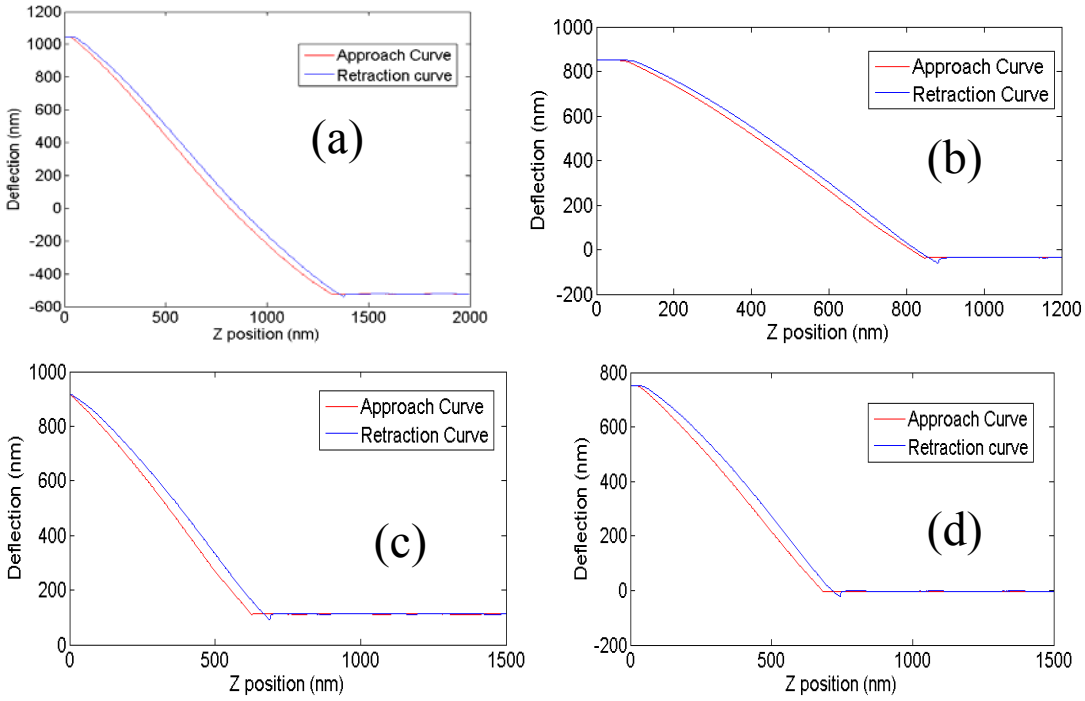

Figure 5 – 2. Typically observed deflection-distance curves for pollen grains 4 and 5 on Si: (a) pollen grain 4 at 20% relative humidity; (b) pollen grain 4 at 60% relative humidity; (c) pollen grain 5 at 20% relative humidity; (d) pollen grain 5 at 60% relative humidity. The plateaus at 0 nm Z position indicate the limit of the Nanoscope IIIa photodetector for our applied loads, and the grains were subjected to a maximum pressure of about 0.5 GPa for all 4 cases (assuming only one pollen spike is in contact with the surface).

5.3 RESULTS AND DISCUSSIONS

Figure 5 – 3 shows the adhesion forces of the pollen grains 1 – 3 with different polymer substrate surfaces.

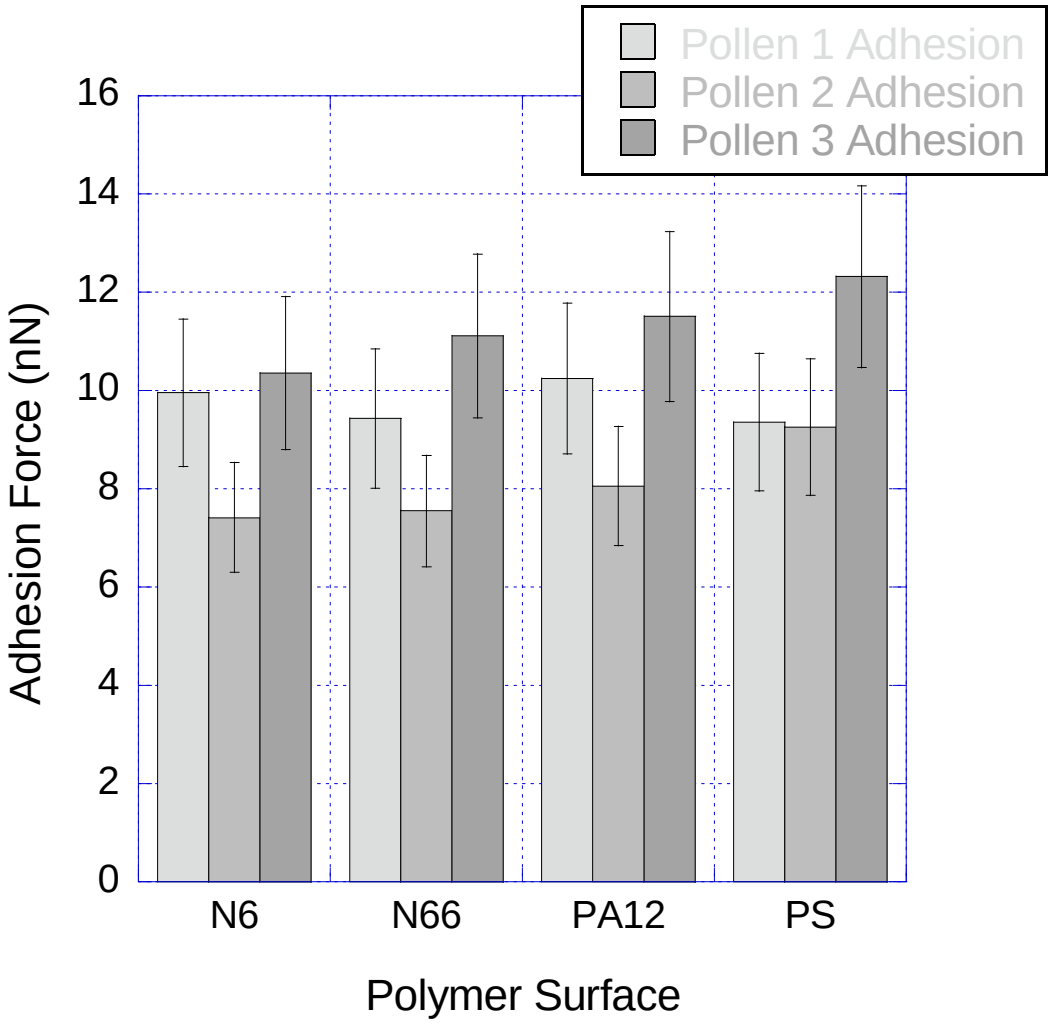

Figure 5 – 3. Bar graphs of the adhesion forces between the pollen attached AFM tips with various polymer surfaces at 95% confidence level.

They range between 7 nN and 13 nN, and adhesive forces for all 3-different pollen grains for the same surface overlap with one exception (grains 2 and 3 on all 4

polymer surfaces). It is most notable that there is no significant difference in adhesion force for the same pollen grain with different polymer substrates. Adhesive interactions and elastic deformation are related, especially in the case of compliant sample surfaces such as many biological and soft polymer surfaces.[112] However, from our previous AFM study of the same set of polyamides and polystyrene[92], the maximum elastic deformation of the polymer surface had no significant contribution to the adhesion force. Surface roughness, as an indicator of morphology, can have an effect on adhesion. Table 5 – 1 shows the roughness parameters Ra and RMS of the spin coated polymer surfaces.

Table 5 – 1. Surface roughness of the various substrate surfaces. *Note*. Uncertainty is ± 95% confidence interval.

Surface	PA6	PA66	PA 12	PS	Si
Ra (nm)	97.7 ± 15.0	79.7 ± 4.2	5.4 ± 0.9	4.9 ± 0.5	0.2 ± 0.2
RMS (nm)	111.7 ± 18.4	100.3 ± 5.2	7.0 ± 1.3	6.1 ± 1.1	0.3 ± 0.2

If roughness is an important factor, then rougher surfaces such as those of N6 and N66 should exhibit stronger adhesion forces. But as seen in figure 3, this is not the case. PA12 has a smoother surface yet adhesion forces are higher with the pollen grain (though with overlapping error bars) on average than with N66 which is rougher.

Given the unique spiky surface morphology of the ragweed pollen grain, it is possible that that we can have two or more spikes adhering to the polymer substrate surface. In about 10% of cases, we observed the attachment and detachment of 2 pollen spikes to the polymer surface, as shown in Figure 5 – 4.

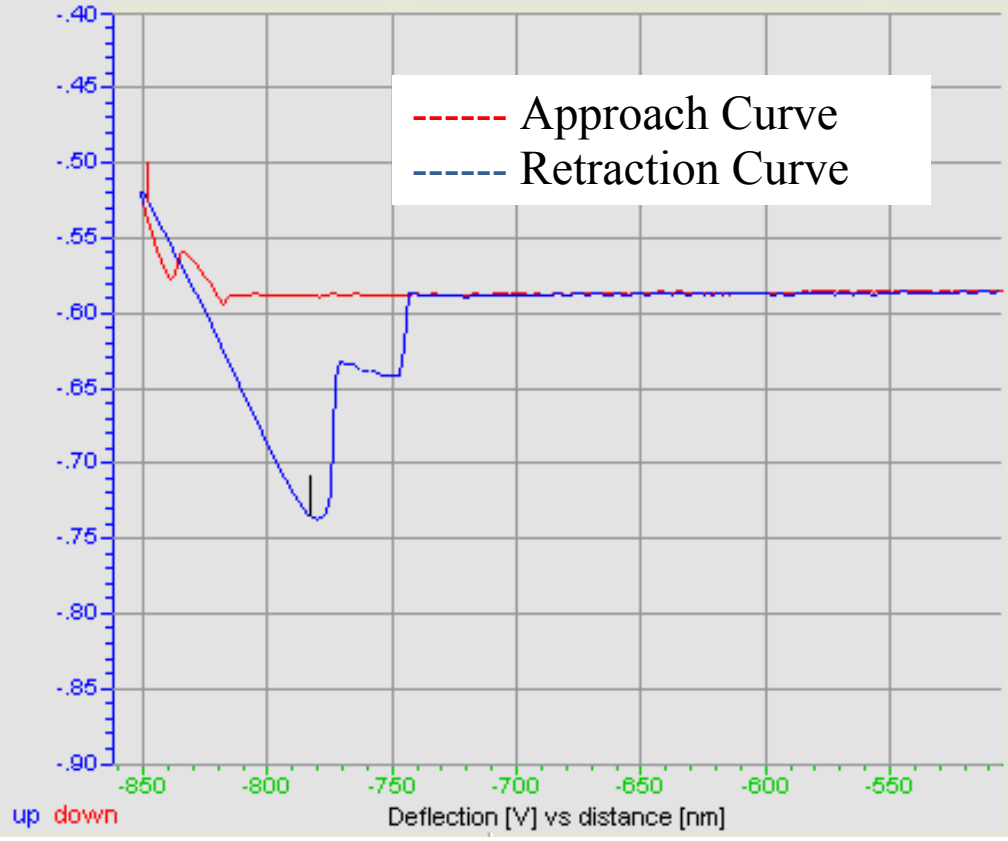

Figure 5 – 4. A deflection-distance curve suggesting sequential attachment and detachment of two pollen spikes to polymer surface. The red and blue vertical lines are markers indicating the maximum and minimum points of the approach and retraction curves.

In nature, pollen presents significant allergenic potential only in the form of respirable-sized proteins smaller than ~1 μm. Such small particles are produced by osmotic rupture when intact pollens (>10 μm) are exposed to water or just simply from the drying of fresh pollen grains as they are released into the atmosphere[113, 114]. These fragments can then be inhaled deeply into the lungs, or capillary and van der Waals forces bind them to larger particles, including intact pollen grains[115]. There are suggestions that these protein-containing particle fragments could present surface chemistry and contact geometry different from the pollen exine surface. In the case of intact ragweed pollen, protein is believed to be transported from the protoplasm to the external environment via pores on the grain surface as seen in Figure 5 – 5[113, 115, 116]. In these cases, proteins might contribute functional groups that could form hydrogen bonds with polyamides.

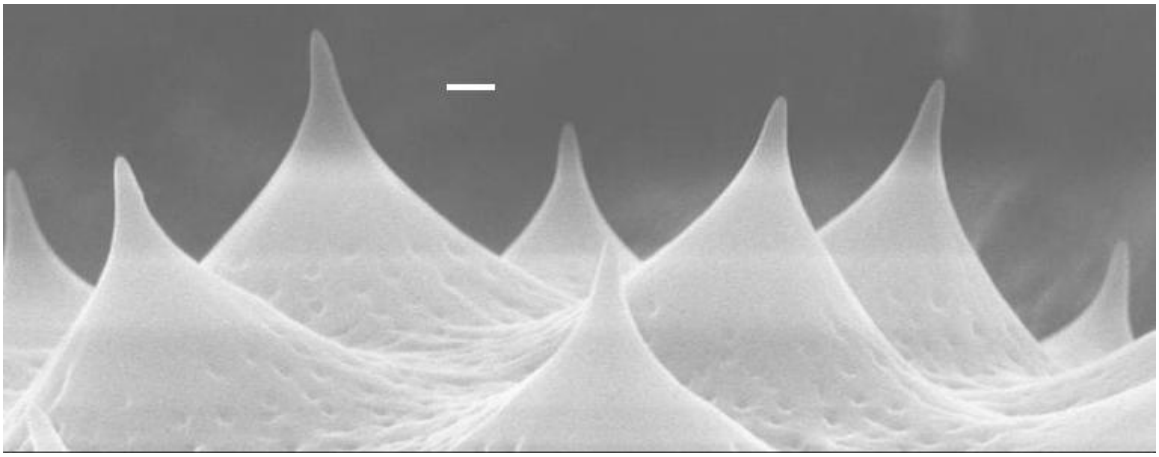

Figure 5 – 5. Electron micrograph of a section of the ragweed pollen grain exine surface after repeated adhesion force measurements with multiple polymer substrates. The white scale bar represents 200nm.

To test for the presence of specific interactions in the adhesion, , we used one of the pollen-attached AFM tips (pollen grain 1) *after* the gold sputtering and SEM imaging to measure the adhesion force with polystyrene of various molecular weights. We also measured the adhesion forces with a hydrophilic piranha-etched Si wafer. Table 5 – 2 shows the static water contact angle of the various substrate surfaces while Figure 5 – 6 presents the adhesion force data of the *gold-coated* pollen AFM tip (pollen grain 1) with PS of varying molecular weights and silicon.

Table 5 – 2. Static water contact angle of the substrate surfaces. *Note*. Uncertainty is ± 95% confidence interval.

Surface	PA6	PA66	PA 12	PS	Si
	75.2 ± 1.0	67.1 ± 0.6	72.8 ± 1.8	90.6 ± 0.7	13.3 ± 0.1

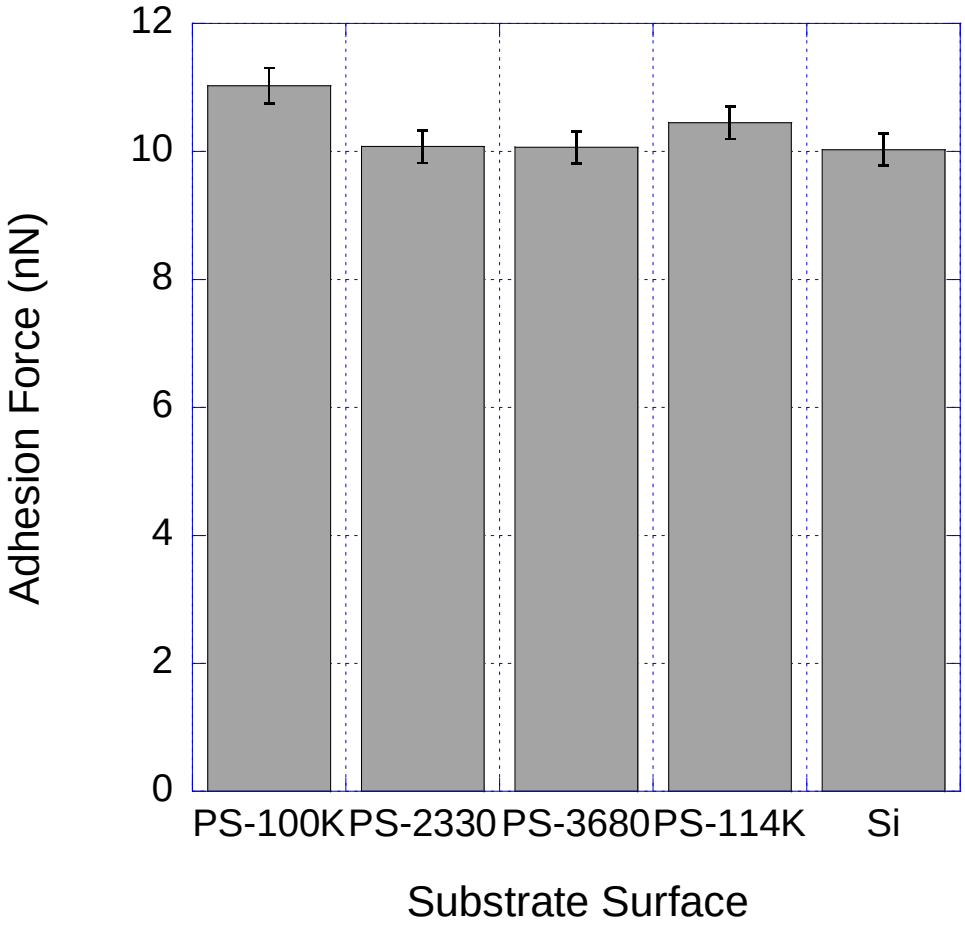

Figure 5 – 6. Bar graphs of the adhesion forces between a gold-coated pollen attached AFM tip (pollen grain 1) with polystyrene of varying molecular weights and silicon at 95% confidence level.

The combination of this second set of pollen AFM direct force measurements with the first set from Figure 5 – 3 supports the hypothesis that pollen generally adhere to natural surfaces mainly via non-specific intermolecular (van der Waals) forces. Firstly, there was no significant change in the magnitude of adhesion forces compared to the earlier non-gold coated pollen tip force data, and the forces were approximately constant

for both the polystyrene and silicon surfaces. We had adjusted the voltage during the gold sputtering for SEM imaging such that the gold layer on the pollen grain is very thin (< 5 nm) and this would remove any specific interactions on the pollen surface and not van der Waals forces. We did not see any evidence of electrostatic interactions. The force approach and retraction curves did not overlap entirely and there was the distinct jump of the tip from the surface upon retraction at the pull-off distance where there is no net attractive or repulsive force between the tip and the substrate surface. Thirdly, if specific interactions were governing, the adhesion forces after gold sputtering should be significantly different from that prior to the gold coating. The gold layer would have presumably prevented the short-range contact with the substrate surface necessary for specific interactions. But in the case of the PS with MW = 100,000, the adhesion forces remained about the same before and after gold sputtering. Lastly, from Figure 2 the hydrophilic piranha-etched Si surface had similar adhesion forces with the pollen tip, indicating that capillary forces from 20% – 40% relative humidity do not play a very significant role in dry pollen adhesion to surfaces. The big difference in the water contact angles in Table 2 and similar adhesion forces across the different polymer surfaces do not favor a capillary mechanism and there is no decrease in adhesion forces for the hydrophobic PS compared to piranha-etched hydrophilic silicon. Capillary forces may play a role when relative humidity is greater than 60% (which is the humidity limit for our experimental set-up) and on hydrophilic surfaces[117].

We varied the molecular mass of polystyrene used as a substrate to see if polymer chain entanglement or surface hardness is a factor in adhesion. As molecular mass drops

from 100000 to 1000, the glass transition temperature of polystyrene drops dramatically from ~100 C to ~38 C.[118] From Figure 5 – 6, there is no conclusive evidence to suggest this might be happening since PS of different molecular weights generates adhesion forces which are not significantly different from one another.

Van der Waals forces are the weakest of all intermolecular forces, but are universally present.[42] Adhesion to any surface utilizing just non-specific van der Waals interactions alone is possible. However, a large number of these interactions would have to be present simultaneously between two surfaces to generate a strong enough adhesive force relative to the size of the smaller object. This means contact area between the two surfaces must be maximized. As shown in figures 1 and 5, the spiked geometry characteristic of ragweed pollen exine may have been Nature's way to use pollen wall morphology combined with weak intermolecular forces, rather than specific chemistry, for adhesion. Further, the SEM micrograph (Figure 5 – 5) does not show any noticeable wearing or chipping of the pollen spikes during the repeated adhesion force measurements. This can be inferred by measurements with different tips which show similar adhesion behavior with no strong dependence on the particular pollen-tip chosen. The highly compressive tests in Figure 5 – 2 show the resilience and strength of the pollen exine structure. Given that the typical ragweed pollen is spherical in nature, such a design increases rather than reduces the force of adhesion as it increases the number of contact points. After all, a perfect sphere has only one point of contact with a flat surface.

If we assume that the tip of the spike of the pollen grain is a hemisphere (radius, R ~ 17 nm, from Figure 5 – 5), and is separated by a distance D from an infinitely large, flat surface, we can estimate the adhesion force of one exine spike to the surface by[42]:

$$F = \frac{A_H R}{6D^2} \qquad (5-1)$$

Where A_H is the material dependent non-retarded Hamaker constant and for bioparticles it is typically 0.5 – 2 x 10^{-19} J for interactions in air[31]; D = 0.165 nm the nominal value used for cut-off separation. This theoretical estimate gives an adhesion force for an exine spike to be between 5 - 20 nN. From Figure 5 – 3, our ragweed pollen grain has an average measured adhesion force of about 7 – 13 nN, which is well within the range of the predicted adhesion forces. These values, together with the deflection-distance curve in Figure 5 – 4 support the contention that only one or at most two spikes are in contact with a flat surface at a given moment, and that a rough surface will increase adhesion. Given the limitations of our knowledge about the exine spike morphology, orientation upon contact with a surface as well as its material (optical and dielectric) properties, our 'colloidal' probe method allows us to determine the adhesion force of a single pollen exine spike accurately by utilizing the AFM.

The pollen exine represents the outer layer of the grain and is composed of sporopollenin, a complex polymer consisting of carboxylic acid groups joined to saturated and unsaturated aliphatic chains with varying amounts of aromatics[119-121]. We would expect that dispersion (London) forces will be the primary interaction between the pollen grain with the various surfaces. As a result, it is not surprising that the adhesion

forces across the various surfaces are similar in magnitude, even after the gold coating (Figure 5 – 7). While the exact thickness of the sputtered gold coating on the pollen AFM tip is not known, it was less than 10 nm (and within the range of van der Waals interactions). The adhesion forces did not change significantly when the gold was present.

How might this dependence on van der Waals forces for adhesion by pollen aid us in providing useful design principles for indoor carpet and upholstery materials? Ragweed pollen grains, like gecko setae[122-126], adhere to surfaces depending mainly on surface contact geometry rather than on surface chemistry. More work can be done with regards to minimizing pollen adhesion to surfaces. While surface hydrophobicity is no guarantee of adhesion or repulsion as shown above, materials such as fluorohydrocarbons serve as promising candidates to minimize pollen adhesion.

5.4 CONCLUSIONS

We have shown here that ragweed pollen grains adhere primarily by geometry rather than surface chemistry, but questions remain as to their contact morphology with substrate surfaces and how this relates to their strong surface adhesive forces. Our estimates show that van der Waals forces account for the bulk of the measured adhesion, with negligible contributions from capillary forces. Characterization of low surface energy materials that serve as promising candidates for the manufacture of self-cleaning

carpet will be necessary before we can address the issue of protective and preventive measures to minimize the negative impact of pollen allergens indoors.

CHAPTER VI

CONCLUSIONS AND RECOMMENDATIONS FOR FUTHER STUDY

6.1 CONCLUSIONS

The purpose of this research was to use the atomic force microscope (AFM) to measure adhesion forces between selected relevant bioparticles (such as *E. coli* bacteria and ragweed pollen grains) and surfaces consisting of a series of polyamides (PA6, PA66 and PA12) and polystyrene (PS), materials that are prominent in carpeting, upholstery, and other indoor surfaces. This work showed how information about the work of adhesion, contact radii at the particle – polymer interface and Hamaker constants of the probe – surface interactions could be extracted from adhesion force measurements.

First, a measurement technique was developed to quantify the adhesive interactions between polymeric carpeting materials. The probe tips were coated with the polymers using a micropipette containing the dilute polymer solution attached to a micromanipulator. Adhesive forces were measured between the AFM tips (polymer – coated and unmodified) and planar surfaces of the same series of polymers. Several interesting characteristics were observed from the force – distance measurements. All adhesion forces were in the range of 1.5 – 8 nN, with the weakest force observed for an unmodified AFM tip with a PS surface and the strongest between a PS – coated tip and a

PS surface. Adhesion forces between the two most dissimilar (PA6 – PS and PA66 – PS) materials were found to be significantly asymmetric – the forces were different depending on the relative placement of each polymer on the AFM tip or substrate. Materials with similar chemistry and intermolecular interactions yielded forces in close agreement regardless of placement on the AFM tip or substrate.

Calculation of the tip – substrate surface contact radii was done by using the experimental forces via four models: Derjaguin, Muller, and Toporov (DMT); Johnson, Kendall, and Roberts (JKR); parametric tip – force distance relation (PT/FDR) and a square-pyramid-flat-surface (SPFS) model developed herein. The SPFS model was found to give the most reasonable contact tip radius estimate, falling in the range that is typically reported for tip radii in AFM force – distance measurements. Hamaker constants calculated from the SPFS model using this radius agreed in both magnitude and trends with experiment and Lifshitz theory.

This approach of using polymer-coated AFM tips to measure polymer – polymer adhesion forces was then extended to quantify the adhesive interactions of *E. coli* immobilized on a substrate with the polymer-coated AFM tips. The adhesion forces for the tip-bacterial interactions were in the range between 2.9 and 6.7 nN, which is of the same magnitude as the polymer-polymer interactions for the same series of polymers. Polystyrene had stronger adhesion with *E. coli* than any of the three polyamides, by an average factor of 1.4. One of the plausible reasons is the presence of carbohydrate – aromatic interactions between the bacterium cell surface and PS aromatic rings. The work

of adhesion and Hamaker constants of the probe – surface interactions were calculated using the SPFS model.

For the study of the adhesive behavior of short ragweed pollen grains to polymers, single pollen grains were attached to the free end of a tip – less AFM cantilever. Humidity and pollen compliance were investigated as potential artifacts, but were shown to be insignificant under the measurement conditions. A typical pollen grain had an average adhesion force of 10 ± 3 nN to a flat polymer surface, independent of surface type. We conclude that van der Waals forces are the primary mechanism for adhesion and that the number of contacts formed, and hence the total force, is controlled by the presence of spiky growths on the pollen surface.

The AFM provided reliable, quantitative and reproducible adhesion force data for the selected bioparticles and polymer substrate surfaces, and information on additional parameters such as the work of adhesion, contact radii at the particle – polymer interface and Hamaker constants of the probe – surface interactions could be easily extracted from the adhesion force measurements. The AFM can be used to help develop accurate adhesion contact models based on a fundamental understanding of particle affinities with polymers utilized in carpet and as a characterization tool for the development of newer carpet materials that can provide a cleaner indoor air environment.

6.2 RECOMMENDATIONS FOR FUTURE WORK

The AFM has been used to probe the nanoscale adhesive interactions between a diverse variety of surfaces as it is a useful tool for adhesion characterization. The research presented here shows how the 'coated-tip' and 'colloidal probe' methods, applied in this work for the measurement of *E. coli* and ragweed pollen adhesion to polymers respectively, makes it possible to measure micron-sized particle interactions with surfaces. It would be interesting to investigate if similar methodologies could be implemented to other bioparticles of interest such as fungi spores and other types of bacteria and pollen which are of different surface geometries and to develop suitable contact geometry adhesion models to describe their adhesion and release profiles.

For decades, manufacturers have chemically-treated carpet to impart resistance to water, soil, and oil-based staining. Anti-soiling treatments function by limiting the wettability of water and oils, and by reducing the adhesion of solid soil particles. The treatments nowadays are dominated by the addition of perfluoroalkyl compounds[127] through co-polymerization with the hydrocarbon co-monomers. Maximum repellency is achieved with polymers with perfluoroalkyl side chains containing more than 7 carbons. Fibers are also adjusted make it harder as harder fibers show reduced contact area and hence lower adhesion energy with solid particles. Commercial treatments have been reviewed by Kissa[128]. The quantitative impact of bioparticle adhesion to such fluoropolymers is unclear, and the AFM 'colloidal probe' method is well suited to

conduct a detailed contact mechanics analysis on the effectiveness of the fluoropolymers in minimizing bioparticle adhesion be it bacteria, pollen grains or fungi spores.

Nylon fibers present a special challenge, as even with fluorochemical anti-soil treatments, permanent staining is possible if staining agents are not removed quickly. This occurs due to chemisorptions of acid dyes prevalent in foods and beverages onto Nylon's amine end groups. In the 1980s DuPont and other manufacturers began to commercialize stain-blocking treatments based on anionic hydrocarbons such as phenol-formaldehydes (syntans), styrene-maleic acid copolymers, and methacrylic acid copolymers added during spinning or as a post-mill finish of Nylon. These polymers diffuse into the filaments to block Nylon end groups from acid staining agents. Details of the adsorption of such commercial formulations on Nylons have been discussed elsewhere[129]. The influence of the anionic stain-blocking agents on the adhesion of bioparticulates is less clear, mainly due to the presence of numerous functional groups on the typically-used stain blockers. They may play a role by modifying the adhesion with Nylon or by countering the expected diminished adherence due to the fluoroalkyls. It would be interesting to see if there is any significant change in adhesion forces between bioparticles with these modified carpet polymers from the unmodified nylon.

Finally, there is no method currently that incorporates differences between particle species, fiber treatments, or particle fragments into indoor air quality models. Opportunities thus exist in using the AFM to set up a database of adhesion forces and

further humankind's understanding of the adhesive energy required to release particles from carpet and its impact on respiratory health.

REFERENCES

1. Jones, A. P., Indoor Air Quality and Health. *Atmospheric Environment* **1999,** *33*, 4535 - 4564.

2. Eggleston, P. A., Methods and effectiveness of indoor environmental control. *Annals of Allergy, Asthma and Immunology* **2001,** *87* (1), 44 - 47.

3. Eggleston, P. A., and Bush, R. K., Environmental allergen avoidance: An overview. *J. Allergy and Clinical Immunology* **2001,** *107* (3), 403 - 405.

4. Warner, J. A., Controlling indoor allergens. *Pediatric Allergy and Immunology* **2008,** *11* (4), 208 - 219.

5. http://www.lungusa.org/air (accessed June 2005).

6. *Trends in Asthma Morbidity and Mortality*; American Lung Association Epidemiology and Statistics Unit, Research and Scientific Affairs: March 2003, 2003.

7. EPA Document #402-K-93-007. (6604J), U. S. E. P. A. a. t. U. S. C. P. S. C. O. o. R. a. I. A., Ed. 1995.

8. A.M. Pope, R. P., and H. Burge, *Indoor Allergens: Assessing and Controlling Adverse Health Effects*. National Academy Press: 1993.

9. Betts, K., Are U.S. Homes a Haven for Toxins? *Environ. Sci. Technol.* **2003,** *37* (21), 407A - 411A.

10. United States, E. P. A., and the Consumer Product Safety Commission Office of Radiation and Indoor Air (6604J) *EPA Document #402-K-93-007*; 1995.

11. 2001 National health Interview Survey. Statistics, N. C. f. H., Ed. 2001.

12. K.B Weiss, P. J. G., and T.A. Hodgson, An Economic Evaluation of Asthma in the U.S. *The New England Journal of Medicine* **1992,** *326*, 862.

13. Samet, J., Environmental controls and lung disease. *American Review of Respiratory Disease* **1990,** *142* (4), 915 - 938.

14. D.M. Mannino, D. M. H., C.A. Pertowski, A. Ashizawa, L.L. Nixon, C.A. Johnson, L.B. Ball, E. Jack and D.S. Kang Surveillance for Asthma - United States, 1960 - 1995. Morbidity and Mortality Weekly Report. CDC, Ed. 1998. <http://www.cdc.gov/mmwr/preview/mmwrhtml/00052262.htm>.

15. K. Foarde, M. B., Comparison of bio-contaminant levels associated with hard vs. carpet floors in non-problem schools: Results of a year long study. *J. Exposure Analysis and Environ. Epidemiology* **2004,** *14*, S41 - 48.

16. Jacobs, B. The History of Carpet. http://www.carpetinfo.co.uk/pages/aboutpp/history.htm (accessed June 2005).

17. Cham, R. M. S. R., Effect of flooring on standing comfort and fatigue. *Human Factors* **2001,** *43* (3), 381 - 391.

18. Hatch, K. L., *Textile Science*. West Publishing Minneapolis/Saint Paul, 1993.

19. Yeager, J., *Textiles for residential and commercial interiors*. Harper & Row New York, 1988.

20. Davidsen, J., Carpet and the Environment. *Interior Design* **1995,** *66* (14), S28 - 31.

21. Ackler, H. D., French, R. H., Chiang, Y. M, Comparisons of Hamaker Constants for Ceramic Systems with Intervening Vacuum or Water: From Force Laws and Physical Properties. *J. Colloid and Interface Science* **1996,** *179*, 460 - 469.

22. N. Hollen, J. S., A.L. Langford & S.J. Kadolph, *Textiles*. Macmillan New York, 1988.

23. Antron, Why Dupont Chose Type 6,6 Nylon. E.I. du Pont de Nemours and Company: 2000.

24. Tate, M. L., Kamath, Y. K., Wesson, S. P., and Ruetsch, S. B., Surface Energetics of Nylon 66 Fibers. *J. Colloid and Interface Sci.* **1996,** *177* (2), 579 - 588.

25. Lee, Y., and Char, K., Enhancement of Interfacial Adhesion between Amorphous Polyamide and Polystyrene by in-Situ Copolymer Formation at the Interface. *Macromolecules* **1994,** *27* (9), 2603 - 2606.

26. Boucher, E., Folkers, J. P., Creton, C., Hervet, H., and Léger, L., Enhanced Adhesion between Polypropylene and Polyamide-6: Role of Interfacial Nucleation of the β-Crystalline Form of Polypropylene *Macromolecules* **1997,** *30* (7), 2102 - 2109.

27. C.A. Janeway, P. T., M. Walport, M. Shlomchik, *Immunobiology*. Garland Publishing New York, 2001.

28. Goldsby RA, K. T., Osborne BA and Kuby J *Immunology*. 5th ed.; W.H. Freeman and Company: New York, 2003.

29. AAAAI Tips to Remember: What is an Allergic Reaction? <http://www.aaaai.org/patients/publicedmat/tips/whatisallergicreaction.stm> (accessed June 2005).

30. AAAAI Tips to Remember: Prevention of Allergies and Asthma in Children. <http://www.aaaai.org/patients/publicedmat/tips/preventioninchildren.stm> (accessed June 2005).

31. Thio, B. J., Meredith, C.J., Quantification of *E. coli* Adhesion to Polyamides and Polystyrene with Atomic Force Microscopy. *Colloids and Surfaces B: Biointerfaces* **2008,** *65* (2), 308 - 312.

32. Thio, B. J., Lee, J.H. Meredith, C.J., Characterization of ragweed pollen adhesion to polyamides and polystyrene using atomic force microscopy. *Langmuir* **2008,** *to be submitted*.

33. Heckl, W. M., *Scanning the thread of Life*. R. Piper GmbH &Co: Munich, 1995.

34. G. Binnig, C. F. Q. a. C. G., Atomic Force Microscope. *Physical Review Letters* **1986,** *56*, 930 - 933.

35. Dufrene, Y. F., Atomic Force Microscopy, a Powerful Tool in Microbiology. *Journal of Bacteriology* **2002,** *184* (19), 5205 - 5213.

36. E. Meyer, H. H., P. Grutter, T. Jung, T. Weisskopf, H.R. Hidber, R. Lapka, H. Rudin and H.J. Guntherodt, Comparative Study of lithium fluoride and graphite by atomic force microscopy (AFM). *Journal of Microscopy* **1988,** *152* (1), 269 - 280.

37. A.V. Bolshakova, O. I. K., I.V. Yaminsky, Microbial Surfaces Investigated Using Atomic Force Microscopy. *Biotechnol. Prog.* **2004,** *20* (6), 1615 - 1622.

38. S. Allen, X. C., J. Davies, M.C. Davies, A.C. Dawkes, J.C. Edwards, C.J. Roberts, J. Sefton, S.J.B. Tendler and P.M. Williams, Detection of Antigen-Antibody Binding Events with the Atomic Force Microscope. *Biochemistry* **1997,** *36*, 7457 -7463.

39. F. Podczeck, J. M. N., M.B. James, Influence of relative humidity of storage air on the adhesion and autoadhesion of micronized particles to particulate and compacted powder surfaces. *J. Colloid Interface Sci.* **1997,** *187*, 484 - 491.

40. Rumpf, H., *Agglomeration 77*. American Institute of Mining, Metallurgical and Petroleum Engineers: New York, 1977.

41. Zimon, A. D., *Adhesion of Dust and Powders*. Consultants Bureau: New York, 1982.

42. Israelachvili, J., *Intermolecular and Surface Forces*. 2nd ed.; Academic Press: London, 1992.

43. Lifshitz, E. M., The theory of molecular attractive forces between solids. *Soviet Phys. JETP* **1956,** *2* (1), 73 - 83.

44. Myers, D., *Surfaces, Interfaces, and Colloids: Principles and Applications*. VCH Publishers: New York, 1991.

45. Podczeck, F., *Particle-Particle Adhesion in Pharmaceutical Powder Handling*. Imperial College Press: 1999.

46. Feldman, K., Tervoort, T., Smith, P. and Spencer, N.D, Toward a Force Spectroscopy of Polymer Surfaces. *Langmuir* **1998,** *14*, 372 - 378.

47. N.A Burnham, R. J. C., *Force Spectroscopy*. VCH Publishers: New York, 1993.

48. K. Feldman, T. T., P. Smith and N.D. Spencer, Toward a Force Spectroscopy of Polymer Surfaces. *Langmuir* **1997,** *14*, 372 - 378.

49. R. Jones, H. M. P., J.A.S. Cleaver and C.S. Hodges, Adhesion Forces between Glass and Silicon Surfaces in Air Studied by AFM: Effects of Relative Humidity, Particle Size, Roughness and Surface Treatment. *Langmuir* **2002,** *18*, 8045 - 8055.

50. J.C. Hooton, C. S. G., S. Allen, M.C. Davies, C.J. Roberts, S.J.B. Tendler and P.M. Williams, An Atomic Force Microscopy Study of the Effect of Nanoscale Contact Geometry and Surface Chemistry on the Adhesion of Pharmaceutical Particles. *Pharmaceutical Research* **2004,** *21* (6), 953 - 961.

51. R.G Horn, D. T. S., Contact electrification and adhesion between dissimilar materials. *Science* **1992,** *256*, 362 - 364.

52. L.O. Heim, S. E., M. Preuss and H.J. Butt, Adhesion Forces between individual gold and polystrene particles. *J. Adhesion Sci. Technol.* **2002,** *16* (7), 829 - 843.

53. Buckton, G., *Interfacial Phenomena in Drug Delivery and Targeting*. Harwood Academic Publishers: Switzerland, 1995.

54. Tabor, D. A., A simple theory of static and dynamic hardness. *Proc. Roy. Soc. A* **1948,** *192*, 247 - 274.

55. Fernández-Alonso, M. C., F. J. Cañada, J. Jiménez-Barbero & G. Cuevas, Molecular Recognition of Saccharides by Proteins. Insights on the Origin of the Carbohydrate-Aromatic Interactions. *J. Am. Chem. Soc* **2005,** *127* (20), 7379 - 7386.

56. Midtiby, H. http://en.wikipedia.org/wiki/Young%27s_modulus (accessed 6/6/2005).

57. Hertz, H., On the contact of elastic solids. *J. Reine und Angewandte Mathematik* **1882,** *92*, 156 - 171.

58. K.L. Johnson, K. K. A. D. R., Surface energy and the contact of elastic solids. *Proc. R. Soc. Lond. A* **1971,** *324*, 301 - 313.

59. B.J. Briscoe, K. K. L., D.R. Williams, Adhesive contact deformation of a single microelastomeric sphere. *J. Colloid Interface Sci.* **1998,** *200*, 256 - 264.

60. B.V. Derjaguin, V. M. M., Y.P. Toporov, Effect of contact deformations on the adhesion of particles. *J. Colloid Interface Sci.* **1975,** *53* (2), 314 - 326.

61. J.C. Hooton, C. S. G., S. Allen, M.C. Davies, C.J. Roberts, S.J.B. Tendler and P.M. Williams, Characterization of Particle-Interactions by Atomic Force Microscopy: Effect of Contact Area. *Pharmaceutical Research* **2003,** *20* (3), 508 - 514.

62. N.A. Burnham, D. D. D., R.L. Mowery, R.J Colton, Probing the Surface Forces of Monolayer Films with an Atomic Force Microscope. *Physical Review Letters* **1990,** *64* (16), 1931 - 1934.

63. Maugis, D., Adhesion of spheres: The JKR-DMT transition using a dugdale model. *J. Colloid and Interface Sci.* **1992,** *150*, 243 - 269.

64. Argento, C., French, R. H., Parametric tip model and force-distance relation for Hamaker constant determination from atomic force microscopy. *J. Appl. Phys.* **1996,** *80* (11), 6081 - 6090.

65. Kern, W., Overview and Evolution of Semiconductor Wafer Contamination and Cleaning Technology. In *Handbook of Semiconductor Wafer Cleaning Technology*, Kern, W., Ed. William Andrew Publishing: 1993.

66. Meredith, J. C., Karim, A., Amis, E.J., High Throughput Measurement of Polymer Blend Phase Behavior. *Macromolecules* **2000,** *33*, 5760 - 5762.

67. Meredith, J. C., Smith, A.P., Karim, A., Amis, E.J., Combinatorial Materials Science for Polymer Thin-Film Dewetting. *Macromolecules* **2000,** *33*, 9747 - 9756.

68. Podczeck, F., Newton, J.M., James, M.B., Influence of Relative Humidity of Storage Air on the Adhesion and Autoadhesion of Micronized Particles to Particulate and Compacted Powder Surfaces. *J. Colloid and Interface Sci.* **1997,** *187*, 484 - 491.

69. Li, X., B.E Logan, Analysis of Bacterial Adhesion Using a Gradient Force Analysis Method and Colloid Probe Atomic Force Microscopy. *Langmuir* **2004,** *20*, 8817 - 8822.

70. Cappella, B., Baschieri, P., Frediani, C., Miccoli, P., Ascoli, C., Force-Distance Curves by AFM. *IEEE Engineering in Medicine and Biology* **1997,** *16* (2), 58 - 65.

71. Hoh, J. H., Engel, A., Friction Effects on Force Measurements with an Atomic Force Microscope. *Langmuir* **1993,** *9*, 3310 - 3312.

72. Hues, S. M., Draper, C.F., Lee, K.P., Colton, R.J., Effect of PZT and PMN actuator hysteresis and creep on nanoindentation measurements using force microscopy. *Rev. Sci. Instrum.* **1994,** *65* (5), 1561 - 1565.

73. Brandrup, J. I., Edmund H.; Grulke, Eric A.; Abe, Akihiro; Bloch, Daniel R., *Polymer Handbook, 4th Edition*. John Wiley & Sons: 1999; p V121 - V133.

74. Sedin, D. L., Rowlen, K.L., Adhesion Forces Measured by Atomic Force Microscopy in Humid Air. *Analytical Chemistry* **2000,** *72* (10), 2183 - 2189.

75. Hu, J., Xiao, X.D., Ogletree, D. F., Salmeron, M., Imaging the Condensation and Evaporation of Molecularly Thin Films of Water with Nanometer Resolution. *Science* **1995,** *268* (5208), 267 - 269.

76. Thundat, T., Zheng, X.Y., Chen, G.Y., Sharp, S.L., Warmack, R.J., Characterization of atomic force microscope tips by adhesion force measurements. *Appl. Phys. Lett.* **1993,** *63*, 2150 - 2152.

77. Heim, L. O., Ecke, S., Preuss, M. and H.J. Butt, Adhesion Forces between individual gold and polystrene particles. *J. Adhesion Sci. Technol.* **2002,** *16* (7), 829 - 843.

78. Eastman, T., Zhu, D.M., Adhesion Forces between Surface-Modified AFM Tips and a Mica Surface. *Langmuir* **1996,** *12* (11), 2859 - 2862.

79. Dufrene, Y. F., Recent progress in the application of atomic force microscopy imaging and force spectroscopy to microbiology. *Current Opinion in Microbiology* **2003,** *6*, 317 - 323.

80. Allison, D. P., Hinterdorfer, P., Han, W., Biomolecular force measurements and the atomic force microscope. *Current Opinion in Biotechnology* **2002,** *13*, 47 - 51.

81. Vezenov, D. V., Noy, A., Ashby, P., Chemical Force Microscopy: probing chemical origin of interfacial forces and adhesion. *J. Adhesion Sci. Technol.* **2005,** *19* (3 - 5), 313 - 364.

82. Dunlap, W. C. J., Watters, R.L., Direct Measurement of the Dielectric Constants of Silicon and Germanium. *Physical Review* **1953,** *92* (6), 1396 - 1397.

83. Van Zeghbroeck, B., *Principles of Semiconductor Devices*. University of Colorado: 2004.

84. Sze, S. M., *Physics of Semiconductor Devices* Wiley-Interscience: New York, 1981.

85. Unertl, W. N., Implications of contact mechanics models for mechanical properties measurements using scanning force microscopy. *J. Vac. Sci. Technol. A* **1999,** *17* (4), 1779 - 1786.

86. Xie, R., A. Karim, J.F. Douglas, C.C Han, R.A Weiss, Spinodal Dewetting of Thin Polymer Films. *Physical Review Letters* **1998,** *81* (6), 1251 - 1254.

87. Tsui, O. K. C., Wang, Y.J., Zhao, H., Du, B., Some views about the controversial dewetting morphology of polystyrene films. *Eur. Phys. J. E* **2003,** *12*, 417 - 425.

88. Ducker, W. A., Senden, T.J., Pashley, R.M., Direct measurement of colloidal forces using an atomic force microscope. *Nature* **1991,** *353* (6341), 239 - 241.

89. Assemi, S., Nalaskowski, J., Johnson, W. P., Direct force measurements between carboxylate-modified latex microspheres and glass using atomic force microscopy. *Colloids and Surfaces A: Physicochem. Eng. Aspects* **2006,** *286*, 70 - 77.

90. Bowen, W. R., Hilal, N., Lovitt, R.W., Wright, C.J., Direct measurement of the force of adhesion of a single biological cell using an atomic force microscope. *Colloids and Surfaces A: Physicochemical and Engineering Aspects* **1998,** *136* (1 - 2), 231 - 234.

91. Wright, C. J., Armstrong, I., The application of atomic force microscopy force measurements to the characterisation of microbial surfaces. *Surf. Interface Anal.* **2006,** *38*, 1419 - 1428.

92. Thio, B. J., Meredith, C.J., Measurement of polyamide and polystyrene adhesion with coated-tip atomic force microscopy. *J. Colloid and Interface Science* **2007,** *314* (1), 52 - 62.

93. Amro, N. A., P.K. Lakshmi, K. Wadu-Mesthrige, A. Bulychev, S. Mobashery, and G.Y Liu, High-Resolution Atomic Force Microscopy Studies of the *Escherichia coli* Outer Membrane: Structural Basis for Permeability. *Langmuir* **2000,** *16*, 2789 - 2796.

94. Emsley, J., Very strong hydrogen bonding. *Chem. Soc. Rev.* **1980,** *9*, 91 - 124.

95. Quiocho, F. A., Carbohydrate-Binding Proteins: Tertiary Structures and Protein-Sugar Interactions. *Ann. Rev. Biochem.* **1986,** *55*, 287 - 315.

96. Clarke, C., Woods, R.J., Gluska, J., Cooper, A., Nutley, M.A., Boons, G-J., Involvement of Water in Carbohydrate-Protein Binding. *J. Am. Chem. Soc* **2001,** *123* (49), 12238 - 12247.

97. Lundquist, J. J., and Toone, E.J., The Cluster Glycoside Effect. *Chem. Rev.* **2002,** *102* (2), 555 - 578.

98. Kitov, P. I., and D. R. Bundle, D.R. , On the Nature of the Multivalency Effect: A Thermodynamic Model. *J. Am. Chem. Soc.* **2003,** *125* (52), 16271 - 16284.

99. Nishio, M., Umezawa, Y., Hirota, M., Takeuchi, Y., The CH/pi Interaction: Significance in Molecular Recognition. *Tetrahedron* **1995,** *51* (32), 8665 - 8701.

100. Martin, R. E., Bouwer, E.J., and Hanna, L.M., Application of Clean-Bed Filtration Theory to Bacterial Deposition in Porous Media. *Environ. Sci. Technol.* **1992,** *26* (5), 1053 - 1058.

101. Eichhorn, R., Small, S., Experiments on the lift and drag of spheres suspended in a Poiseuille flow. *J. Fluid Mech.* **1964,** *20* (3), 513 - 527.

102. Welty, J., Wicks, C. E., Wilson, R. E., Rorrer, G. L., *Fundamentals of Momentum, Heat, and Mass Transfer*. John Wiley & Sons: 2001.

103. Weiss, K. B., Gergen, P.J.,and Hodgson, T.A., An Economic Evaluation of Asthma in the U.S. *The New England Journal of Medicine* **1992,** *326*, 862.

104. Weiss, K. B., Sullivan, S.D., The health economics of asthma and rhinitis. I. Assessing the economic impact. *J. Allergy and Clinical Immunology* **2001,** *107* (1), 3 - 8.

105. Monn, C., Exposure assessment of air pollutants: a review on spatial heterogeneity and indoor/outdoor/personal exposure to suspended particulate matter, nitrogen dioxide and ozone. *Atmospheric Environment* **2001,** *35*, 1 - 32.

106. Behrendt, H., Becker, W-M., Localization, release and bioavailability of pollen allergens: the influence of environmental factors. *Current Opinion in Immunology* **2001,** *13* (6), 709 - 715.

107. Traidl-Hoffmann, C., Kasche, A., Menzel, A., Jakob, T., Thiel, M., Ring, J., Behrendt, H., Impact of Pollen on Human Health: More than Allergen Carriers? *Int Arch Allergy Immunol* **2003,** *131*, 1 - 13.

108. Solomon, W. R., Airborne pollen: A brief life. *Journal of Allergy and Clinical Immunology* **2002,** *109* (6), 895 - 900.

109. Binnig, G., Quate, C.F., and Gerber, C., Atomic Force Microscope. *Physical Review Letters* **1986,** *56*, 930 - 933.

110. Burnham, N. A., Chen, X., Hodges, C.S., Matei, G.A., Thoreson, E.J., Roberts, C.J., Davies, M.C and Tendler, S.J.B., Comparison of calibration methods for atomic-force microscopy cantilevers. *Nanotechnology* **2003,** *14*, 1 - 6.

111. Hutter, J. L., and Bechhoefer, J., Calibration of atomic-force microscope tips. *Rev. Sci. Instrum.* **1993,** *64* (7), 1868 - 1873.

112. Sun, Y., Akhremitchev, B., Walker, G. C., Using the Adhesive Interaction between Atomic Force Microscopy Tips and Polymer Surfaces to Measure the Elastic Modulus of Compliant Samples. *Langmuir* **2004,** *20*, 5837 - 5845.

113. Howlett, B. J., Knox, R.B., Heslop-Harrison, J., Pollen-Wall Proteins: Release of the Allergen Antigen E from Intine and Exine Sites in Pollen Grains of Ragweed and Cosmos. *J. Cell Sci* **1973,** *13*, 603 - 619.

114. Knox, B., Suphioglu, C., Environmental and molecular biology of pollen allergens. *Trends in Plant Science* **1996,** *1* (5), 156 - 164.

115. Knox, R. B., Pollen Wall Proteins: Pollen-Stigma Interactions in Ragweed and Cosmos (Compositae). *J. Cell Sci* **1973,** *12*, 421 - 443.

116. Piffanelli, P., Ross, J. H. E., Murphy, D. J., Biogenesis and function of the lipidic structures of pollen grains. *Sex Plant Reprod* **1998,** *11*, 65 - 80.

117. Xiao, X., Qian, L., Investigation of Humidity-Dependent Capillary Force. *Langmuir* **2000,** *16* (21), 8153 - 8158.

118. Dibenedetto, A. T., Dilandro, L., Correlation of Glass Transition Temperature and Molecular Weight: A Model Based on the Principle of Corresponding States. *J. Polymer Sci: Part B: Polymer Physics* **1989,** *27*, 1405 - 1417.

119. Dominguez, E., Mercado, J. A., Quesada, M. A., Heredia, A., Pollen sporopollenin: degradation and structural elucidation. *Sex Plant Reprod* **1999,** *12*, 171 - 178.

120. Ivleva, N. P., Niessner, R., Panne, U., Characterization and discrimination of pollen by Raman microscopy. *Anal Bioanal Chem* **2005,** *381* (1), 261 - 267.

121. Kano, H., Hamaguchi, H., Vibrational Imaging of a Single Pollen Grain by Ultrabroadband Multiplex Coherent Anti-Stokes Raman Scattering Microspectroscopy. *Chemistry Letters* **2006,** *35* (10), 1124 - 1125.

122. Tian, Y., Pesika, N., Zeng, H., Rosenberg, K., Zhao, B., McGuiggan, P., Autumn, K., Israelachvili, J., Adhesion and friction in gecko toe attachment and detachment. *Proc. Natl. Acad. Sci. USA* **2006,** *103* (51), 19320 - 19325.

123. Huber, G., Gorb, S. N., Spolenak, R., Arzt, E., Resolving the nanoscale adhesion of individual gecko spatulae by atomic force microscopy. *Biol. Lett.* **2005,** *1*, 2 - 4.

124. Autumn, K., Peattie, A. M., Mechanisms of Adhesion in Geckos. *Integr. Comp. Biol.* **2002,** *42* (6), 1081 - 1090.

125. Autumn, K., Liang, Y. A., Hsieh, S. T., Zesch, W., Chan, W. P., Kenny, T. W., Fearing, R., Full, R. J., Adhesive force of a single gecko foot-hair. *Nature* **2000,** *405*, 681 - 685.

126. Zhao, B., Pesika, N., Rosenberg, K., Tian, Y., Zeng, H., McGuiggan, P., Autumn, K., Israelachvili, J., Adhesion and Friction Force Coupling of Gecko Setal Arrays: Implications for Structured Adhesive Surfaces. *Langmuir* **2008,** *24* (4), 1517 - 1524.

127. Rao, N. S., and Baker, B.E., *Organofluoride Chemistry: Principles and Commercial Applications*. Plenum Press: New York, 1994.

128. Kissa, E., *Handbook of Fiber Science and Technology*. Marcel Dekker: New York, 1984; Vol. II.

129. Burkinshaw, S. M., Gotsopoulos, A., The adsorption of a commercial stainblocker on nylon 6.6. *Journal of Applied Polymer Science* **2000,** *77* (14), 3062 - 3068.